PLL- and FLL-Based Speed Estimation Schemes for Speed-Sensorless Control of Induction Motor Drives: Review and New Attempts

Huimin Wang, *Student Member, IEEE*, Yongheng Yang, *Senior Member, IEEE*, Xinglai Ge, *Member, IEEE*, Yun Zuo, *Student Member, IEEE*, Yan Yue, and Songtao Li

***Abstract*—Phase-locked loops (PLLs) and frequency-locked loops (FLLs) are of importance in power and energy applications. Both technologies have been introduced to speed-sensorless- controlled motor drives, and increasing applications of PLLs and FLLs for speed estimation are foreseen. To enable a proper and good design, a thorough review of the PLL- and FLL-based speed estimation schemes is then provided in this article. It is revealed through the review that many PLL- and FLL-based estimation schemes fail to accurately track a frequency ramp (i.e., obvious estimation errors appear), which may lead to a compromised estimation accuracy when these schemes that are applied in induction motor drives operating during acceleration and deceleration processes. To address this, the proven speed estimation schemes together with new attempts are also presented in this article. Moreover, various challenges to the PLL- and FLL-based speed estimation schemes, including harmonics, dc offsets, and parameter variations, are considered when evaluating these schemes. Solutions to tackle these disturbances are accordingly presented. In addition, two representative estimation schemes are exemplified through experimental tests. Finally, further challenges in using the PLL- and FLL-based schemes for speed estimation are discussed.**

***Index Terms*—DC offsets, frequency-locked loop (FLL), harmonics, induction motor drives, parameter estimation, phase-locked loop (PLL), speed estimation, speed-sensorless control.**

NOMENCLATURE

v_α, v_β	α- and β-axis components of the inputs.
v_d, v_q	d- and q-axis components of the inputs.
θ, ω	Phase and frequency of the inputs
V, φ	Amplitude and initial phase of the inputs
$\hat{\theta}$	Estimated phase of the inputs.
$\hat{\omega}$	Estimated frequency of the inputs.
$\hat{V}$	Estimated amplitude of the inputs.
$\hat{\varphi}$	Estimated initial phase of the inputs.
θ_e	Phase estimation error.
k_p, k_i	Gains of the loop filter in the PLL scheme.
$\hat{v}_\alpha$, $\hat{v}_\beta$	Estimated signals of the inputs.
$q\hat{v}_\alpha$,$q\hat{v}_\beta$	Quadrature terms of the estimated signals.
k, Γ	Gains of the SOGI-FLL scheme.
$\varepsilon_{e\alpha}$, $\varepsilon_{e\beta}$	α- and β-axis components of synchronization error.
$\varepsilon_{f\alpha}$, $\varepsilon_{f\beta}$	α- and β-axis components of frequency error.
k_R, λ	Gains in the ROGI-FLL scheme.
$\Psi_{r\alpha}$, $\Psi_{r\beta}$	α- and β-axis components of the rotor flux.
R_s	Stator resistance.
R_r	Rotor resistance.
L_s	Stator inductance.
L_r	Rotor inductance.
L_m	Magnetizing inductance.
$T_r = L_r/R_r$	Rotor time constant.
ω_r	Rotor speed.
ω_{sl}	Slip speed.
$\boldsymbol{u_s} = [u_{s\alpha}\ u_{s\beta}]^T$	Stator voltage vector.
$\boldsymbol{i_s} = [i_{s\alpha}\ i_{s\beta}]^T$	Stator current vector in the stationary reference frame.
$\boldsymbol{i_{sdq}} = [i_{sd}\ i_{sq}]^T$	Stator current vector in the synchronous reference frame.
$\boldsymbol{e_s} = [e_{s\alpha}\ e_{s\beta}]^T$	Stator back EMFs.
$\Psi_{\boldsymbol{s}}^{\boldsymbol{i}} = [\Psi_{s\alpha}{}^{i}\ \Psi_{s\beta}{}^{i}]^T$	Stator flux vector in the current model (CM).
$\Psi_{\boldsymbol{r}}^{\boldsymbol{i}} = [\Psi_{r\alpha}{}^{i}\ \Psi_{r\beta}{}^{i}]^T$	Rotor flux vector in the CM.
$\hat{\boldsymbol{\Psi}}_{\mathbf{s}}^{\mathbf{v}} = [\hat{\Psi}_{s\alpha}^{v}\ \hat{\Psi}_{s\beta}^{v}]^T$	Stator flux vector in the voltage model (VM).

Manuscript received October 12, 2020; revised January 28, 2021, May 10, 2021, and August 1, 2021; accepted September 28, 2021. Date of publication October 6, 2021; date of current version November 30, 2021. This work was supported in part by the High-Speed Railway Joint Funds of the National Natural Science Foundation of China under Grant U1934204 and in part by the National Natural Science Foundation of China under Grant 52177060. Recommended for publication by Associate Editor S.-C. Yang. (*Corresponding author: Xinglai Ge*.)

Huimin Wang, Xinglai Ge, Yun Zuo, Yan Yue, and Songtao Li are with the Ministry of Education Key Laboratory of Magnetic Suspension Technology and Maglev Vehicle, Southwest Jiaotong University, Chengdu 610031, China (e-mail: wanghuimin@my.swjtu.edu.cn; xlge@swjtu.edu.cn; z_uoy_un@my.swjtu.edu.cn; ystone@my.swjtu.edu.cn; songtaoli@my.swjtu.edu.cn).

Yongheng Yang is with the College of Electrical Engineering, Zhejiang University, Hangzhou 310027, China (e-mail: yang_yh@zju.edu.cn).

Color versions of one or more figures in this article are available at https://doi.org/10.1109/TPEL.2021.3117697.

Digital Object Identifier 10.1109/TPEL.2021.3117697

$\hat{\boldsymbol{\Psi}}_r^{\mathbf{v}} = [\hat{\Psi}_{r\alpha}^{v}\ \hat{\Psi}_{r\beta}^{v}]^T$	Rotor flux vector in the VM.
$\Psi_{\boldsymbol{sdq}}{}^{\boldsymbol{i}} = [\Psi_{sd}{}^{i}\ \Psi_{sq}{}^{i}]^T$	Stator flux vector in the CM in the synchronous reference frame.
$\Psi_{\boldsymbol{rdq}}{}^{\boldsymbol{i}} = [\Psi_{rd}{}^{i}\ \Psi_{rq}{}^{i}]^T$	Rotor flux vector in the CM in the synchronous reference frame.
$\boldsymbol{e_{scom}} = [e_{scom\alpha}\ e_{scom\beta}]^T$	Compensation signals of the stator back EMFs in the VM.
$\Psi_{\boldsymbol{scom}} = [\Psi_{scom\alpha}\ \Psi_{scom\beta}]^T$	Compensation signals of the stator flux in the VM.
$\boldsymbol{G} = [g_1\ g_1]^T$	Gain matrix of the full-order observer with the sliding mode (SM) method (FSMO).
$\hat{\theta}_r$	Estimated rotor flux phase.
$\mathrm{sgn}(\cdot)$	Sign function.
$e^{j\hat{\theta}_r} = \cos\hat{\theta}_r + j\sin\hat{\theta}_r$	Euler's formula.
$\xi_{\alpha\beta n}$	Inputs in the sub-structure of the adaptive filters.

I. Introduction

INDUCTION motors have been widely used due to their comparative advantages in terms of low manufacturing cost, convenient system maintenance, and high operation performance. In most of induction motor drives, speed information should make a feedback to control system. This task is generally carried out by using speed sensors. The use of speed sensors, however, brings several concerns, e.g., reduce system reliability, increase system costs, and require extra installation space. Hence, speed-sensorless control, implemented by various speed estimation schemes, is increasingly demanded in induction motor drives [1]–[3].

Generally, speed estimation schemes applied in induction motor drives can be categorized into two groups: the nonideal-phenomena-based schemes and the model-based schemes. The nonideal-phenomena scheme can be conducted through signal injection [4]–[7] and rotor slot harmonic extraction [8]–[11]. Although the non-ideal-phenomena-based schemes perform well in a wide speed range and they are insensitive to parameter variations, such schemes may result in certain side-effects on induction motor drives, e.g., obvious torque ripples and unnecessary power losses [3]. Moreover, the general drawbacks of difficult signal extraction and poor flexibility further hinder the practical applicability.

The model-based schemes perform speed estimation on the basis of induction motor model [12]–[42]. It means that this type of speed estimation schemes is dependent on induction motor parameters. Accordingly, these schemes may suffer from unsatisfactory estimation performance due to parameter variations. Nevertheless, such schemes have been thriving, as they are easy to be implemented and flexible to be adjusted. Basically, the model-based estimation schemes are implemented by employing various observers, e.g., the adaptive full-order observer (AFO) [12]–[18], the adaptive reduced-order observer (ARO) [19]–[21], the extended Kalman filter (EKF) [22]–[24], and the sliding mode observer (SMO) [25]–[30]. In addition, the model reference adaptive system (MRAS) based methods are attractive among assorted model-based schemes for being simple and requiring low computational efforts [31]–[35]. Among them, in [13], an improved AFO was proposed for speed-sensorless-controlled induction motor drives, in which the gain matrix was deliberately designed to provide strong robustness against disturbances. As followed, Chen and Huang [15] first presented a review of the AFO-based schemes with stator and rotor resistances identification for induction motor drives. Then, a new attempt of the AFO scheme with simultaneous stator and rotor resistances estimation was accordingly made, in which a stability analysis for stable operation was provided. A novel speed-sensorless method based on the ARO for induction motor drives was reported in [19]. In this scheme, the flux estimation was absent, which simplifies the overall system and parameter tuning. Moreover, according to the singular perturbation theory, the stability analysis of the proposed speed estimator was also given in [19]. In [21], an ARO was used for speed-sensorless control of induction motors. In this scheme, the observer gain design for analytical stability was elaborated. Additionally, a stator resistance adaptation was used to guarantee speed estimation with parameter variations. In [24], a thorough performance comparison of the optimized EKFs using different fitness functions for speed-sensorless-controlled induction motor drives was presented. Here, the differential evolution algorithm and the multiobjective differential evolution algorithm were adopted, respectively, instead of the complex covariance matrices. By doing so, accurate speed estimation and computational burden reduction are achieved. A concept of time-division multiplexing was incorporated to observer design in [27] for induction motor drives, and consequently, an SMO was obtained for flux estimation. With this, the instability problem caused by bounded disturbances was addressed. A second-order SMO scheme was accomplished in [29] for linear induction motor drives. In this scheme, accurate speed estimation and chattering behavior alleviation were obtained. Moreover, a parallel stator resistance on-line identification was employed to deal with the issue of stator resistance variations. Furthermore, a review of the MRAS-type schemes for motor drives was made in [32], in which a detailed introduction of various MRAS-based schemes and the stability analysis of these schemes were provided. Also, speed estimation can be achieved by using the advanced control methods, e.g., the particle swarm optimization method [36], the fuzzy control method [37], [38], the genetic algorithm [39], the artificial neural network (ANN) method [40], [41], and the nonlinear control method [42]. As for the advanced control-based techniques, most of them have shown high effectiveness in speed estimation, but certain issues, e.g., high computational burden and system complexity, remain to be resolved.

In power and energy applications, synchronous reference frame-phase-locked loops (SRF-PLLs) have been widely used to extract the phase, frequency, and amplitude of the fundamental component of the grid voltage, accomplishing the task of synchronization [43]–[45]. This key characteristic makes it especially suitable as a speed estimator in sensorless control of motor drives [46]–[59]. Consequently, considerable attempts have been made toward the SRF-PLL-based schemes for sensorless-controlled motor drives. Many of the attempts are put on enhancing the disturbance attenuation capability of the SRF-PLL-based schemes and their variants [46]–[52]. This is

because the SRF-PLL schemes have an insufficient capability to mitigate disturbances. For example, harmonics in the SRF-PLL scheme may lead to apparent ripples in the estimated parameters, and consequently, the estimation accuracy is degraded. Notably, most of the existing SRF-PLL schemes can be regarded as a type-2 control system with a proportional-integral (PI) controller-based loop filter. That means, these schemes may lose the capability of accurately tracking frequency ramps. As a result, the SRF-PLL schemes applied in motor drives may present estimation errors during acceleration and deceleration processes, where the frequency undergoes a ramp change. This may be a serious problem in certain applications that require induction motor to frequently work during acceleration and deceleration processes.

Alternatively, the synchronization can be achieved in power and energy applications through frequency-locked loops (FLLs) [62]–[71]. Among them, the second-order generalized integrator-frequency-locked loop (SOGI-FLL) [62]–[68] and the reduced-order generalized integrator-frequency-locked loop (ROGI-FLL) [69]–[71] are notable FLL examples. Similar to the SRF-PLL schemes, the SOGI-FLL and the ROGI-FLL schemes are promising candidates in speed estimation for motor drives. Unfortunately, the frequency ramp is still a challenging issue for most of the existing SOGI-FLL and ROGI-FLL schemes, when being applied in motor drives to achieve speed estimation.

In light of the above, this article presents a review of the proven PLL schemes with new attempts using the FLL schemes to address the concern when experiencing frequency ramps. In Section II, the implementations of the prior-art PLL- and FLL-based schemes are first presented. Meanwhile, the estimation performance of these schemes during frequency ramps is thoroughly analyzed. The analysis shows that most of the existing PLL- and FLL-based schemes are unable to track frequency ramps accurately. Following that, the improved PLL-based schemes, e.g., the type-3 PLL schemes and the dual-loop PLL schemes, to tackle the challenge of frequency ramps are detailed in Sections III. However, in most of the improved PLL schemes, concerns like system dynamics degradation and stability margin reduction remain to be addressed. Due to this, attempts of employing the FLL technology are explored in Sections IV and V. Moreover, considering disturbances, e.g., harmonics, dc offsets, and parameter variations, may make performance deterioration on speed estimation in practice, considerable solutions to eliminate disturbances have also been developed, which are shown in Section VI, and several typical examples of these solutions are exemplified. A case study is given in Section VII to investigate the performance of two representative estimation schemes through experimental tests. Finally, Section VIII concludes this article.

II. Performance Analysis of the Existing PLL- and FLL-Based Schemes

In this section, a review of the existing PLL- and FLL-based schemes is performed, and the performance of these estimation schemes during frequency ramps is also analyzed.

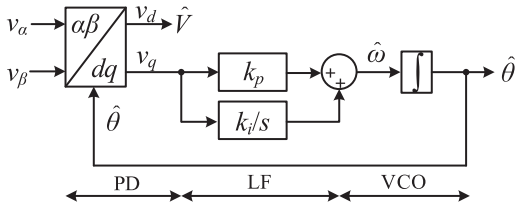

Fig. 1. Block diagram of the SRF-PLL scheme that is composed of a PD, an LF, and a VCO.

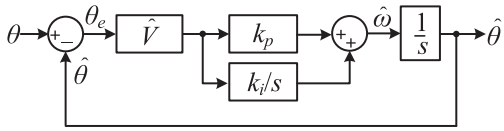

Fig. 2. Small-signal model of the SRF-PLL scheme.

A. SRF-PLL Scheme

In power and energy applications, the SRF-PLL scheme, as shown in Fig. 1, is the most common synchronization method. More importantly, this scheme, as a speed estimator for motor drives, also attracts much popularity. As seen in Fig. 1, the SRF-PLL scheme includes a phase detector (PD), a loop filter (LF), and a voltage-controlled oscillator (VCO) [43]–[45]. Accordingly, the small-signal model of the SRF-PLL scheme is depicted in Fig. 2, and the open-loop transfer function is obtained as

$$G_{ol}^{\mathrm{SRF}}(s) = \frac{\hat{\theta}}{\theta - \hat{\theta}} = \frac{\hat{\theta}}{\theta_e} = \hat{V}\frac{k_p s + k_i}{s^2} \tag{1}$$

where $G_{ol}{}^{\mathrm{SRF}}(s)$ is the open-loop transfer function of the SRF-PLL scheme. There are two poles at the origin in (1), suggesting that the SRF-PLL scheme is a type-2 control system. The type-2 control system cannot accurately track a frequency ramp, which is further elaborated as follows. The phase-error transfer function of the SRF-PLL scheme is expressed as

$$G_e^{\mathrm{SRF}}(s) = \frac{1}{1 + G_{ol}^{\mathrm{SRF}}(s)} = \frac{s^2}{s^2 + \hat{V}k_p s + \hat{V}k_i}. \tag{2}$$

When a frequency ramp input (h/s^2) is applied, corresponding to a phase change (h/s^3), that is

$$\Delta\theta_e^{\mathrm{SRF}}(s) = \frac{h}{s^3}G_e^{\mathrm{SRF}}(s) = \frac{1}{s}\frac{h}{s^2 + \hat{V}k_p s + \hat{V}k_i} \tag{3}$$

where $\Delta\theta_e{}^{\mathrm{SRF}}(s)$ and h are the phase-error transfer function with the frequency ramp and the gain of the ramp change, respectively. Applying the final value theorem to (3) yields

$$\Delta\theta_{ess}^{\mathrm{SRF}}(s) = \lim_{s\to 0} s\Delta\theta_{e}^{\mathrm{SRF}}(s) = \lim_{s\to 0} s\frac{h}{s(s^2+\hat{V}k_p s+\hat{V}k_i)} = \frac{h}{\hat{V}k_i} \quad (4)$$

indicating that an estimation error will appear in the SRF-PLL scheme when tracking the inputs with a frequency ramp. Notably, as shown in (4), the estimation error can be reduced by increasing the integral gain of the LF (i.e., k_i), which means the SRF-PLL scheme needs to increase its bandwidth. The consequence of a high-bandwidth SRF-PLL scheme includes the degraded immunity against disturbances, e.g., noise immunity. This is further elaborated as follows. The closed-loop transfer function of the SRF-PLL scheme is given as

$$G_{cl}^{\mathrm{SRF}}(s) = \frac{\hat{\theta}}{\theta} = \frac{\hat{V}k_p s+\hat{V}k_i}{s^2+\hat{V}k_p s+\hat{V}k_i} \quad (5)$$

which can be rewritten as

$$G_{cl}^{SRF}(s) = \frac{\hat{V}k_p s+\hat{V}k_i}{s^2+\hat{V}k_p s+\hat{V}k_i} = \frac{2\zeta\omega_n s+{\omega_n}^2}{s^2+2\zeta\omega_n s+{\omega_n}^2} \quad (6)$$

in which ζ and ω_n are defined as the damping factor and natural frequency, respectively. Based on (6), the amplitude-frequency characteristic of the SRF-PLL scheme can be expressed as

$$\left|G_{cl}^{\mathrm{SRF}}(j\omega)\right| = \left|\frac{{\omega_n}^2+j2\zeta\omega_n\omega}{({\omega_n}^2-\omega^2)+j2\zeta\omega_n\omega}\right|. \quad (7)$$

Then, it can be obtained that

$$\left|G_{cl}^{\mathrm{SRF}}(j0)\right| = \left|\frac{{\omega_n}^2}{{\omega_n}^2}\right| = 1. \quad (8)$$

Therefore, it can be further deduced that

$$\left|G_{cl}^{\mathrm{SRF}}(j\omega_b)\right| = \left|\frac{{\omega_n}^2+j2\zeta\omega_n\omega_b}{({\omega_n}^2-{\omega_b}^2)+j2\zeta\omega_n\omega_b}\right| = \frac{1}{\sqrt{2}}\left|G_{cl}^{\mathrm{SRF}}(j0)\right| \quad (9)$$

with ω_b being the bandwidth frequency of the SRF-PLL scheme, which can be expressed as

$$\omega_b = \omega_n\sqrt{(1+2\zeta^2)+\sqrt{(1+2\zeta^2)^2+1}}. \quad (10)$$

The bandwidth of the SRF-PLL scheme is related to the natural frequency ω_n, for a given damping factor ζ. Moreover, the noise bandwidth of the SRF-PLL scheme is defined as [60], [61]

$$B_n = \frac{1}{2\pi}\int_0^{\infty}\left|G_{cl}^{\mathrm{SRF}}(j\omega)\right|^2 d\omega = \frac{1+4\zeta^2}{8\zeta}\omega_n \quad (11)$$

which indicates that the noise bandwidth is associated with the natural frequency ω_n, when the value of ζ is given. More specifically, a smaller value of ω_n leads to a narrower noise bandwidth, and hence, a better noise immunity; while, the noise immunity of the SRF-PLL scheme is deteriorated with increasing the value of ω_n. It is demonstrated that the estimation error can be reduced by increasing the value of k_i, i.e., increasing the value of ω_n. As a consequence, the system bandwidth as well as the noise bandwidth is increased, which leads to fast dynamics but poor noise immunity.

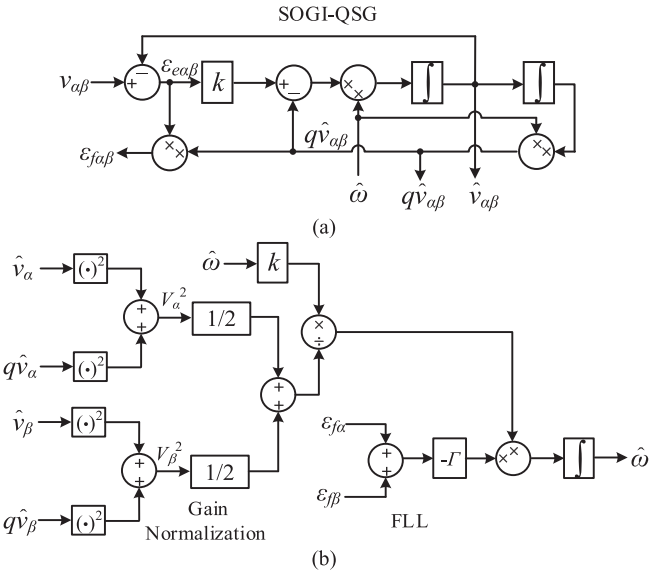

Fig. 3. Block diagram of a typical SOGI-FLL scheme. (a) Second-order generalized integrator-based quadrature-signal generators. (b) FLL with a gain normalization unit.

The inability in tracking frequency ramps accurately is a drawback of the SRF-PLL scheme. This may be a troublesome problem in the applications that require motor to frequently work under acceleration and deceleration cases. Therefore, further attempts should be made to achieve satisfactory estimation, when extending the PLL schemes to motor drives.

B. SOGI-FLL Scheme

The SOGI-FLL scheme is one of the promising synchronization techniques and it is able to achieve satisfactory estimation performance under unbalanced and distorted grid conditions. Moreover, attractive features like acceptable performance and high flexibility make this scheme gain considerable attention. It thus has been employed in many applications, e.g., grid synchronization [62], [63], frequency estimation [64], active damping in *LCL* filter [65], and flux estimation in motor drives [66], [67].

Fig. 3 shows the block diagram of a typical SOGI-FLL scheme, which has two SOGI-based quadrature-signal generators (SOGI-QSGs), a gain normalization unit, and an FLL. In this scheme, the SOGI-QSGs are used to estimate the inputs and their quadrature terms. According to the estimated signals, the FLL achieves frequency estimation. The gain normalization unit is adopted to ensure estimation performance [66]. It is worth noting that, different from the PLL scheme, the SOGI-FLL scheme works in the stationary reference frame. Based on Fig. 3, the frequency characteristic of the SOGI-FLL scheme can be described as

$$\dot{\hat{\omega}} \approx -2\Gamma(\hat{\omega}-\omega). \quad (12)$$

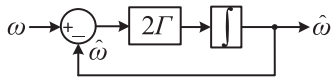

Fig. 4. Simplified model of the FLL scheme.

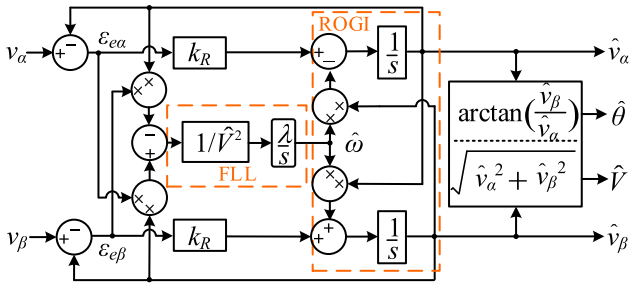

Fig. 5. Block diagram of a typical ROGI-FLL scheme, which includes a ROGI, an FLL, and a polar coordinate transformation.

Then, the simplified model of the SOGI-FLL scheme can be depicted in Fig. 4. According to Fig. 4, the frequency open-loop transfer function can be given as

$$G_{ol}^{\mathrm{SOGI}}(s)=\frac{\hat{\omega}}{\omega-\hat{\omega}}=\frac{2\Gamma}{s}. \tag{13}$$

The frequency-error transfer function is obtained as

$$G_{e}^{\mathrm{SOGI}}(s)=\frac{1}{1+G_{ol}^{\mathrm{SOGI}}(s)}=\frac{s}{s+2\Gamma}. \tag{14}$$

When the inputs have a frequency ramp change (h/s^2), the frequency-error transfer function can be obtained as

$$\Delta\omega_{e}^{\mathrm{SOGI}}(s)=\frac{h}{s^2}G_{e}^{\mathrm{SOGI}}(s)=\frac{h}{s(s+2\Gamma)}. \tag{15}$$

According to the final value theorem, the frequency estimation error of the SOGI-FLL scheme is calculated as

$$\Delta\omega_{ess}^{\mathrm{SOGI}}(s)=\lim_{s\to 0}s\Delta\omega_{e}^{\mathrm{SOGI}}(s)=\lim_{s\to 0}s\frac{h}{s(s+2\Gamma)}=\frac{h}{2\Gamma}\neq 0 \tag{16}$$

which implies that an obvious frequency estimation error appears in the SOGI-FLL scheme with a frequency ramp.

C. ROGI-FLL Scheme

The ROGI-FLL schemes are attractive in three-phase applications acting as synchronization, in which the ROGI unit can perform a similar performance with less computational burden and system complexity than the SOGI-QSGs in the SOGI-FLL scheme [72]–[74].

The block diagram of a typical ROGI-FLL scheme is presented in Fig. 5. As shown in Fig. 5, the ROGI-FLL scheme includes a ROGI, an FLL, and a polar coordinate transformation. The ROGI and the FLL implement the estimations of the inputs and the frequency, respectively. The polar coordinate transformation is employed to estimate the amplitude and the phase of the inputs with the estimated signals. According to Fig. 5, it can

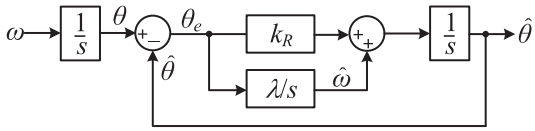

Fig. 6. Simplified model of the ROGI-FLL scheme.

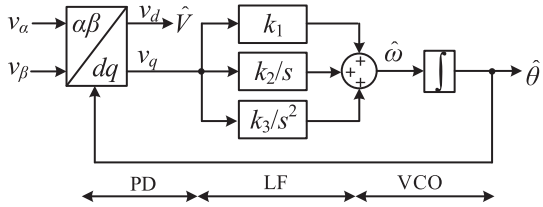

Fig. 7. Block diagram of the type-3 SRF-PLL scheme, where a new LF that has two poles at the origin is employed.

be given that [69]–[71]

$$\begin{cases}\frac{d\hat{\theta}}{dt}=\frac{k_R}{\lambda}\left(\frac{d\hat{\omega}}{dt}\right)+\hat{\omega}\\ \frac{d\hat{\omega}}{dt}=\lambda\sin[(\theta-\hat{\theta})]\approx\lambda(\theta-\hat{\theta})\end{cases}. \tag{17}$$

According to (17), the simplified model of the ROGI-FLL scheme can be obtained, as shown in Fig. 6. Accordingly, the open-loop transfer function of this scheme is obtained as

$$G_{ol}^{\mathrm{ROGI}}(s)=\frac{\hat{\theta}}{\theta-\hat{\theta}}=\frac{\hat{\theta}}{\theta_e}=\frac{k_R s+\lambda}{s^2} \tag{18}$$

which has two poles at the origin, indicating the ROGI-FLL scheme is also a type-2 control system. Similar to the SRF-PLL scheme, the ROGI-FLL scheme may achieve unsatisfactory estimation during frequency ramps (see Section II-A).

It can be summarized from the above analysis that, the issue of frequency ramp challenges most of the existing PLL- and FLL-based speed estimation schemes, including the SRF-PLL scheme, the SOGI-FLL scheme, and the ROGI-FLL scheme. In the following, schemes to address this issue are presented.

III. Improved PLL-Based Schemes

In this section, the improved PLL-based schemes, including the type-3 PLL schemes and the dual-loop PLL schemes, are discussed to perform accurate estimation.

A. Type-3 PLL Schemes

Performance improvement during frequency ramps can be roughly classified into two categories: designing new LF (i.e., type-3 PLL schemes) and increasing system loops (i.e., dual-loop PLL schemes). Type-3 SRF-PLL-based schemes are typical representatives in terms of using a new LF, in which the PI-based LF is replaced by a new LF that has two poles at the origin (that means, this scheme only contains one loop) [75]–[77]. With this, this scheme becomes a type-3 control system that can deal with the frequency ramp issue. The block diagram and the small-signal model of the type-3 SRF-PLL scheme are presented in Figs. 7 and 8, respectively, [note that the unity amplitudes of the inputs are obtained by using an amplitude normalization

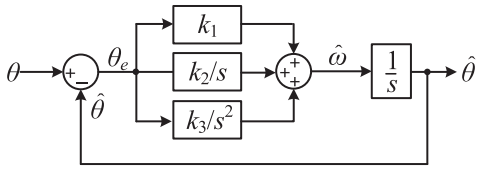

Fig. 8. Small-signal model of the type-3 SRF-PLL scheme, in which k_1, k_2, and k_3 are the gains of the LF.

(AN) unit]. Subsequently, the open-loop transfer function of this scheme is obtained as

$$G_{ol}^{\mathrm{TPLL}}(s) = \frac{\hat{\theta}}{\theta - \hat{\theta}} = \frac{\hat{\theta}}{\theta_e} = \frac{k_1 s^2 + k_2 s + k_3}{s^3} \tag{19}$$

which suggests that, compared to the SRF-PLL scheme, using this new LF induces three poles at the origin in the open-loop transfer function. Thus, the type-3 SRF-PLL scheme in Fig. 7 can ensure accurate estimation with frequency ramps. According to (19), the phase-error transfer function of the type-3 SRF-PLL scheme is written as

$$G_{e}^{\mathrm{TPLL}}(s) = \frac{1}{1 + G_{ol}^{TPLL}(s)} = \frac{s^3}{s^3 + k_1 s^2 + k_2 s + k_3}. \tag{20}$$

The phase-error transfer function of the type-3 SRF-PLL scheme with a frequency ramp (h/s^3) is given as

$$\Delta\theta_e^{\mathrm{TPLL}}(s) = \frac{h}{s^3} G_e^{\mathrm{TPLL}}(s) = \frac{h}{s^3 + k_1 s^2 + k_2 s + k_3}. \tag{21}$$

Using the final value theorem, the phase estimation error with the frequency ramp can be calculated as

$$\begin{aligned} \Delta\theta_{ess}^{\mathrm{TPLL}}(s) &= \lim_{s\to 0} s\Delta\theta_e^{\mathrm{TPLL}}(s) \\ &= \lim_{s\to 0} s \frac{h}{s^3 + k_1 s^2 + k_2 s + k_3} = 0 \end{aligned} \tag{22}$$

which means that the challenge of frequency ramps can be tackled well by using the type-3 SRF-PLL scheme.

Particularly, the newly-designed LF in the type-3 SRF-PLL scheme can be also adopted in the enhanced phase-locked loop (EPLL) scheme [78] and the steady-state linear Kalman filter-based phase-locked loop (SSLKF-PLL) scheme [79]–[81], and accordingly, obtaining their type-3 versions.

B. Dual-Loop PLL Schemes

Alternatively, further attempts to enhance estimation performance by increasing the system loops. That is, a dual-loop PLL scheme is achieved by introducing extra loops into the SRF-PLL scheme. A typical example of the dual-loop PLL schemes is presented in Fig. 9 [82]–[85]. As shown, two tracking loops are employed: Loops 1 and 2. Loop 1 is regarded as a conventional SRF-PLL scheme and loop 2 has a proportional gain (i.e., γ) that acts as an LF. According to the small-signal model of this scheme in Fig. 10, the open-loop transfer function of the dual-loop PLL

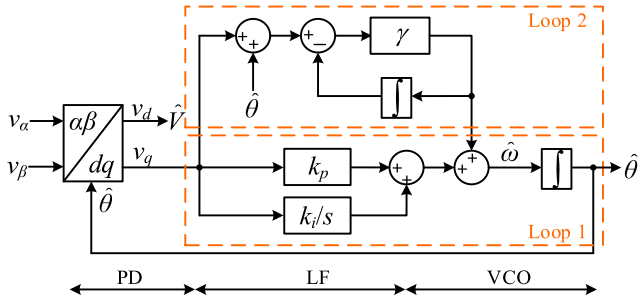

Fig. 9. Block diagram of the dual-loop PLL scheme, which consists of two tracking loops that have their own LF and VCO.

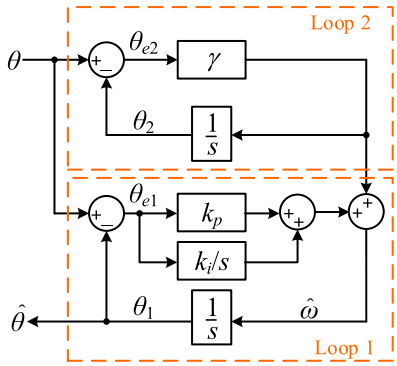

Fig. 10. Small-signal model of a typical dual-loop PLL scheme in Fig. 9, in which θ_1, θ_{e1}, θ_2, and θ_{e2} denote the estimated phase, the phase estimation error in Loop 1, the estimated phase, and the phase estimation error in Loop 2.

scheme is written as

$$\begin{aligned} G_{ol}^{\mathrm{DPLL}}(s) &= \frac{\hat{\theta}}{\theta - \hat{\theta}} = \frac{\hat{\theta}}{\theta_{e1}} \\ &= \frac{(k_p + \gamma)s^2 + (k_i + k_p\gamma)s + k_i\gamma}{s^3}. \end{aligned} \tag{23}$$

The same analysis method can be applied in this dual-loop PLL scheme, and it is suggested that the dual-loop PLL scheme behaves satisfactorily with frequency ramps. Besides, several dual-loop PLL schemes, e.g., the feedforward-loop PLL scheme [86], the improved feedforward-loop PLL scheme [87]–[89], and the high-order PLL scheme (it means that the system order of the PLL scheme is more than 3 by using dual loops) [90], [91], have also been reported in the literature. Notice that, the open-loop transfer function of the type-3 SRF-PLL scheme is identical to that of the dual-loop PLL scheme when assigning $k_1 = k_p + \gamma$, $k_2 = k_i + k_p\gamma$, and $k_3 = k_i\gamma$. That means, the dual-loop PLL scheme can achieve similar performance, compared to that of the type-3 SRF-PLL scheme.

C. Discussions

According to the above analysis, it is interesting to mention that the type-3 PLL schemes and the dual-loop PLL schemes make a performance enhancement during frequency ramps by increasing the system order. These increased-order PLL schemes may tackle the challenge of frequency ramps effectively. However, several issues in terms of stability margin and system

dynamics may appear. For example, one of noticeable problems in the increased-order PLL schemes is the negative gain margin, which is undesired in practice, as demonstrated in the following. Taking the type-3 PLL scheme as an example, the open-loop transfer function of a typical type-3 PLL scheme can be described as

$$G_{ol}(s) = \frac{\hat{\theta}}{\theta - \hat{\theta}} = \frac{\hat{\theta}}{\theta_e} = \frac{as^2 + bs + c}{s^3} \tag{24}$$

where a, b, and c are positive gains, and $ab>c$ (which can be obtained according to the Routh–Hurwitz stability criterion). Then, the open-loop transfer function can be rewritten as

$$G_{ol}(s) = l\frac{(s+\omega_1)(s+\omega_2)}{s^3} \tag{25}$$

where l, ω_1, and ω_2 are the gains of the LF. To simplify the analysis, considering $\omega_1 = \omega_2 = \omega_q$, it can be deduced that

$$G_{ol}(s) = l\frac{(s+\omega_q)^2}{s^3}. \tag{26}$$

Subsequently, the amplitude-frequency and the phase-frequency characteristics of this scheme can be obtained as

$$|A(j\omega)| = |G_{ol}(j\omega)| = l\frac{\omega^2 + {\omega_q}^2}{\omega^3} \tag{27}$$

$$\varphi = \angle G_{ol}(j\omega) = 2\arctan(\frac{\omega}{\omega_q}) - \frac{3}{2}\pi. \tag{28}$$

Based on (27) and (28), the phase margin (PM) and the gain margin (GM) of the type-3 PLL scheme can be given by

$$\mathrm{PM} = \angle G_{ol}(j\omega_c) - (-\pi) = 2[\arctan(\frac{\omega_c}{\omega_q})] - \frac{1}{2}\pi \tag{29}$$

$$\mathrm{GM} = 20\lg[\frac{1}{|G_{ol}(j\omega_g)|}] = 20\lg(\frac{\omega_g}{2l}) \tag{30}$$

where ω_c and ω_g denote the amplitude-crossing frequency and the phase-crossing frequency, respectively, and

$$|G_{ol}(j\omega_c)| = 1 \tag{31}$$

$$\angle G_{ol}(j\omega_g) = -\pi. \tag{32}$$

According to (29)–(32), it can be deduced that

$$\begin{aligned}\mathrm{GM} &= 20\lg(\frac{\omega_g}{2l}) = 20\lg(\frac{\omega_q}{2l}) = 20\lg(\frac{\omega_q}{\omega_c}\times\frac{\omega_c}{2l}) \\ &= 20\lg[\frac{1}{\tan(\mathrm{PM}) + \sec(\mathrm{PM})}\times\frac{1}{\sin(PM)+1}] \\ &= 20\lg\{\frac{\cos(PM)}{[\sin(PM)+1]^2}\}\end{aligned} \tag{33}$$

which indicates that the GM of the type-3 PLL scheme is related to the PM. Generally, the PM of the type-3 PLL scheme is within the range of 40°–50°. It means that the GM is negative in this range (see Fig. 11), which may increase the risk of system instability. Moreover, the increased-order PLL schemes may also lead to slow dynamics. In all, the increased-order PLL schemes may effectively address the concern of frequency ramps. The two main problems, i.e., negative stability margin and poor system dynamics, prevent these schemes from becoming preferable solutions.

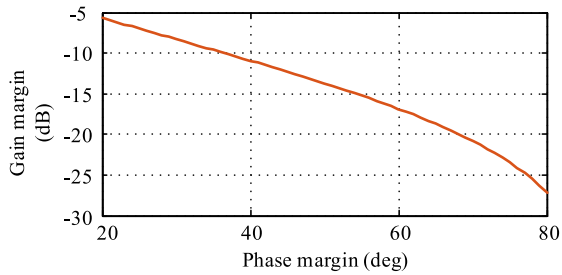

Fig. 11. Relationship between the GM and the PM of the type-3 PLL scheme.

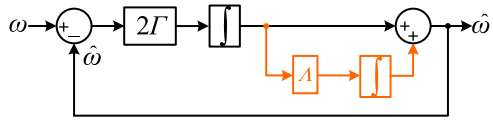

Fig. 12. Simplified model of the SOGI-EFLL scheme ($p = 2\Gamma$, $q = 2\Gamma\Lambda$).

IV. New Attempts of the SOGI-FLL-Based Schemes

The existing SOGI-FLL schemes suffer from performance degradation during frequency ramps. In this section, further efforts have been made to achieve accurate estimation.

A. SOGI-EFLL Scheme

Due to its FLL unit, the conventional SOGI-FLL scheme fails to accurately track a frequency ramp. Hence, a straightforward way to improve speed estimation performance during frequency ramps is re-designing the FLL unit. Assuming the open-loop transfer function of an enhanced FLL (EFLL) unit is a type-2 control system, as

$$G_{ol}^{\mathrm{EFLL}}(s) = \frac{ps+q}{s^2} \tag{34}$$

where p and q are positive gains. Then, the frequency-error transfer function of the EFLL scheme can be given as

$$G_e^{\mathrm{EFLL}}(s) = \frac{1}{1 + G_{ol}^{\mathrm{EFLL}}(s)} = \frac{s^2}{s^2 + ps + q}. \tag{35}$$

The frequency-error transfer function of the EFLL scheme with a frequency ramp (h/s^2) is given as

$$\Delta\omega_e^{\mathrm{EFLL}}(s) = \frac{h}{s^2}G_e^{\mathrm{EFLL}}(s) = \frac{h}{s^2 + ps + q}. \tag{36}$$

Appling the final value theorem, the frequency estimation error of the EFLL scheme with the frequency ramp is obtained as

$$\Delta\omega_{ess}^{\mathrm{EFLL}}(s) = \lim_{s\to 0} s\Delta\omega_e^{\mathrm{EFLL}}(s) = \lim_{s\to 0} s\frac{h}{s^2 + ps + q} = 0. \tag{37}$$

Accordingly, the simplified model and the block diagram of a typical SOGI-EFLL scheme are presented in Figs. 12 and 13, in which Λ and Γ are the gains of the EFLL scheme.

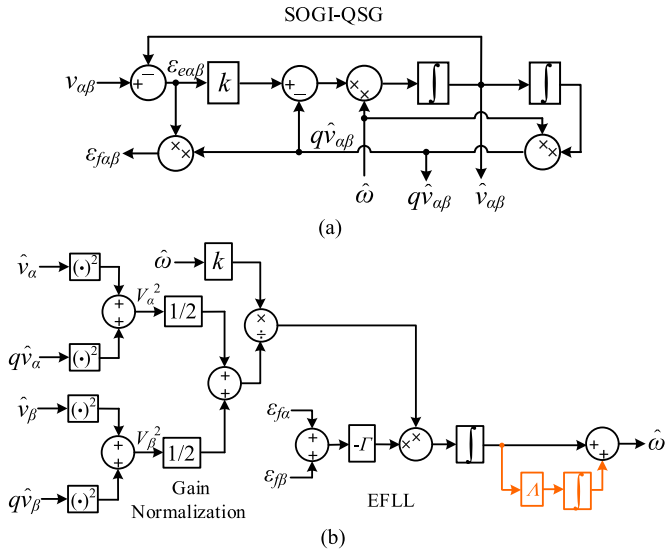

Fig. 13. Block diagram of a typical SOGI-EFLL scheme, in which k, Γ, and Λ are the gains of the SOGI-EFLL scheme. (a) Second-order generalized integrator-based quadrature-signal generators. (b) EFLL with a gain normalization unit.

It should be noted that, the SOGI-EFLL scheme has a few implementation possibilities. For example, a feedforward loop can also be introduced in the SOGI-FLL scheme to achieve the SOGI-EFLL scheme, which is not covered in this article. According to the aforementioned discussions, the SOGI-EFLL scheme may work well during frequency ramps through increasing the system order. Therefore, similar to the increased-order PLL schemes, system dynamics and stability margin are two major concerns associated with the SOGI-EFLL scheme.

B. SOGI-RFLL Scheme

Alternatively, a recommended FLL (RFLL) scheme is accomplished in this section. The estimated frequency can be obtained as

$$\hat{\omega} = \frac{d\hat{\theta}}{dt} = \frac{d}{dt}[\arctan(\frac{\hat{v}_\beta}{\hat{v}_\alpha})]. \tag{38}$$

Subsequently, the estimated frequency can be further deduced that

$$\hat{\omega} = \frac{d}{dt}[\arctan(\frac{\hat{v}_\beta}{\hat{v}_\alpha})] = \frac{\dot{\hat{v}}_\beta \hat{v}_\alpha - \dot{\hat{v}}_\alpha \hat{v}_\beta}{\hat{v}_\alpha^2 + \hat{v}_\beta^2} = \frac{\dot{\hat{v}}_\beta \hat{v}_\alpha - \dot{\hat{v}}_\alpha \hat{v}_\beta}{\hat{V}^2}. \tag{39}$$

Supposing the unity amplitudes of the estimated signals are obtained, that is

$$\hat{V} = 1. \tag{40}$$

Then, the estimated frequency can be calculated as

$$\hat{\omega} = \frac{\dot{\hat{v}}_\beta \hat{v}_\alpha - \dot{\hat{v}}_\alpha \hat{v}_\beta}{\hat{V}^2} = \dot{\hat{v}}_\beta \hat{v}_\alpha - \dot{\hat{v}}_\alpha \hat{v}_\beta. \tag{41}$$

According to (41), the block diagram of the SOGI-RFLL scheme is illustrated in Fig. 14. As shown, in the SOGI-RFLL scheme, an AN unit is involved to provide the unity amplitudes of the inputs. In addition, the estimated signals and their derivatives are provided through the SOGI-QSGs. Eventually, the estimated frequency is obtained from a new-type FLL unit according to the estimated signals. It is worth noticing that, in this scheme, this solution to address the concern of frequency ramps is employing a new FLL unit, rather than increasing the system order. Due to the use of this structure, the stability margin and dynamic performance are maintained. Moreover, the absence of extra system parameters means that the parameter tuning burden will not be increased.

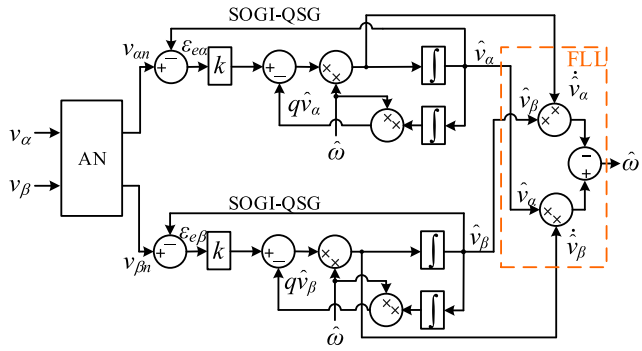

Fig. 14. Block diagram of the SOGI-RFLL scheme, in which a new FLL unit is employed.

C. Discussions

Regarding the SOGI-FLL scheme, new attempts to enhance estimation performance by introducing extra loops into the FLL unit (i.e., the SOGI-EFLL scheme) are made. The performance enhancement performed by the SOGI-EFLL scheme, however, is achieved at the cost of increasing the system order. The increased-order schemes, as discussed previously, may present slow system dynamics and low stability margin. By contrast, the SOGI-RFLL scheme without increasing the system order is a more promising candidate in terms of system dynamics and stability margin. Notably, no extra parameters are introduced into the SOGI-RFLL scheme, and accordingly, this scheme will not bring the concern of parameter tuning.

However, in the SOGI-RFLL scheme, the issue of estimated frequency feedback should be carefully considered. As shown in Fig. 14, in the SOGI-QSGs, the estimated frequency is fed back, being responsible for generating estimated signals. Notice that in the SOGI-RFLL scheme, the frequency estimation is the last step of the entire estimation process. Therefore, several issues like time delays and noise, may affect speed estimation. Moreover, once the estimated frequency is incorrect and fed back into the SOGI-QSGs, the estimations of the inputs are degraded. And in turn, the speed estimation accuracy of the SOGI-RFLL scheme may be further worsened with improper estimated signals.

V. New Attempts of the ROGI-FLL-Based Schemes

The frequency ramp is a concern for the existing ROGI-FLL schemes. In this section, new attempts of the ROGI-FLL schemes are presented to deal with this issue.

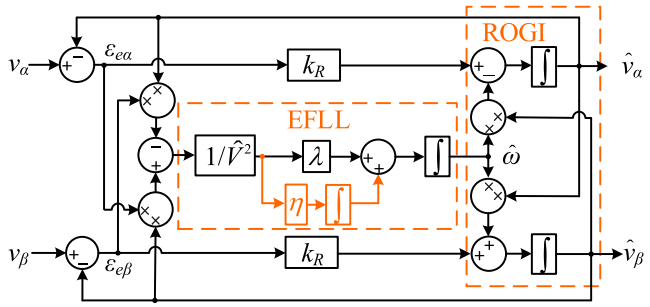

Fig. 15. Block diagram of the ROGI-EFLL scheme, in which k_R, λ, and η are the gains of the ROGI-EFLL scheme.

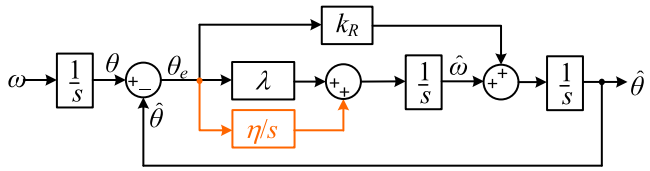

Fig. 16. Simplified model of the ROGI-EFLL scheme.

A. ROGI-EFLL Scheme

The main improvement of the ROGI-EFLL scheme lies in its FLL unit, which can be observed in Fig. 15. As shown, an extra loop is added in the FLL unit of the ROGI-EFLL scheme, and then, the simplified model of this scheme is illustrated in Fig. 16. With this simplified model, the frequency open-loop transfer function of the ROGI-EFLL scheme is written as

$$G_{ol}^{\mathrm{REFLL}}(s) = \frac{\hat{\omega}}{\omega - \hat{\omega}} = \frac{\lambda s + \eta}{s^2(s + k_R)} \tag{42}$$

with k_R, λ, and η being the gains of the ROGI-EFLL scheme. Then, the frequency-error transfer function is expressed as

$$G_{e}^{\mathrm{REFLL}}(s) = \frac{1}{1+G_{ol}^{\mathrm{REFLL}}(s)} = \frac{s^2(s + k_R)}{s^3 + k_R s^2 + \lambda s + \eta}. \tag{43}$$

When applying the frequency ramp input (h/s^2), and then, it can be given as

$$\Delta\omega_{e}^{\mathrm{REFLL}}(s) = \frac{h}{s^2} G_{e}^{\mathrm{REFLL}}(s) = \frac{h(s + k_R)}{s^3 + k_R s^2 + \lambda s + \eta}. \tag{44}$$

According to the final value theorem, it yields

$$\begin{aligned} \Delta\omega_{ess}^{\mathrm{REFLL}}(s) &= \lim_{s\to 0} s\Delta\omega_{e}^{\mathrm{REFLL}}(s) \\ &= \lim_{s\to 0} s\frac{h(s + k_R)}{s^3 + k_R s^2 + \lambda s + \eta} = 0 \end{aligned} \tag{45}$$

indicating that it is available to achieve accurate estimation with a frequency ramp by using the ROGI-EFLL scheme. The ROGI-EFLL scheme, similar to the SOGI-EFLL scheme, performs accurate estimation by introducing an extra loop in the FLL unit. With this, the system order is increased.

As discussed previously, the issues of slow system dynamics and low stability margin remain to be resolved in the ROGI-EFLL schemes.

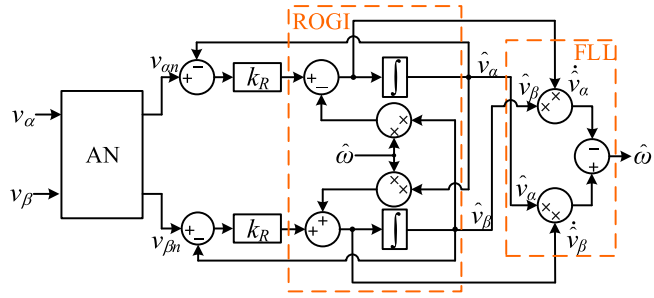

Fig. 17. Block diagram of the ROGI-RFLL scheme.

B. ROGI-RFLL Scheme

Notice that the new-type FLL unit applied in the SOGI-RFLL scheme (see Section IV-B) can be extended into the ROGI-FLL scheme, and thus, achieving the ROGI-RFLL scheme, as shown in Fig. 17. In this scheme, the unity amplitudes of the inputs are obtained by using an AN unit. Afterward, the estimated signals are obtained through the ROGI. The speed estimation is eventually achieved from the new-type FLL unit. Comparing Fig. 14 with Fig. 17, the main difference between the SOGI-RFLL scheme and the ROGI-RFLL scheme is the estimation method of the inputs. That is, the SOGI-QSGs and the ROGI are employed to estimate the inputs in these schemes, respectively. More specifically, compared to the SOGI-RFLL scheme, the ROGI-RFLL scheme requires less implementation complexity and computational efforts but its complex-vector expression leads to the coupling effect.

C. Performance Evaluation

A performance evaluation of the PLL- and FLL-based schemes analyzed in the above is given in Table I. As shown, the estimation performance enhancement during frequency ramps for the PLL-based schemes can be obtained mainly in two ways: designing new LF and introducing additional loops. Most of these schemes can be accepted as the increased-order PLL schemes. Though being effective in enhancing estimation accuracy, the increased-order PLL schemes bring several concerns, including slow dynamic response and negative stability margin. This situation, however, still occurs in the SOGI-EFLL scheme and the ROGI-EFLL scheme. By comparison, the SOGI-RFLL scheme and the ROGI-RFLL scheme are recommended because they address the challenge of frequency ramps without either increasing the system order or introducing extra compensation units. Hence, the SOGI-RFLL scheme and the ROGI-RFLL scheme will not adversely affect system dynamics, stability margin, and parameter tuning. Unfortunately, there is still a problem that has not been resolved yet, i.e., the estimated frequency feedback. As mentioned earlier, the estimated frequency feedback may cause considerable time delays and undesired noise. Moreover, the estimation performance of the RFLL schemes may be further degraded when an inaccurate estimated speed is fedback, which may become a potential issue.

TABLE I
PERFORMANCE EVALUATION OF THE ABOVE-MENTIONED PLL- AND FLL-BASED SCHEMES

Type	Speed estimation scheme name		Ways to achieve accurate estimation	Features	Concerns	Speed-sensorless controlled drives
Improved PLL-based schemes	Type-3 PLL	Type-3 SRF-PLL [75]-[77]	Design new LF	1. Easy implementation 2. Simple structure	1. Slow dynamics 2. Negative gain margin	Available
		Type-3 EPLL [78]				
		SSLKF-PLL [79]-[81]				
	Dual-loop PLL	Dual-loop PLL [82]-[85]	Introduce extra loops			
		Feed-forward PLL [86]-[89]				
		High-order PLL [90], [91]				
New attempts of the FLL-based schemes	EFLL	SOGI-EFLL	Introduce extra loops	1. Easy implementation	1. Slow dynamics 2. Low stability margin	Available
		ROGI-EFLL				
	RFLL	SOGI-RFLL	Employ new FLL unit	1. Easy implementation 2. Adequate stability 3. Acceptable dynamics	1. Frequency feedback	Recommended
		ROGI-RFLL				

VI. IMPLEMENTATION OF THE SPEED ESTIMATION SCHEMES WITH DISTURBANCE ATTENUATION

As known, due to the limited disturbance elimination capability, the PLL- and FLL-based schemes may perform unsatisfactorily when disturbances appear in the inputs (e.g., harmonics, DC offsets, imbalance, voltage sags, swells, etc.). This situation, in motor drives, is still tough. Therefore, the PLL- and FLL-based schemes should incorporate disturbance attenuation schemes to maintain estimation performance. In this section, the implementations of the PLL- and FLL-based schemes with disturbance attenuation will be elaborated. Meanwhile, a few typical examples of disturbance attenuation schemes will be presented.

A. Practical Concerns and Implementations

The PLL- and FLL-based schemes work satisfactorily under an ideal condition, in which the inputs are purely sinusoidal and free from disturbances. This, however, is not always true in induction motor drives due to various disturbances. Notably, the issue of harmonics, which is mainly caused by the inverter nonlinear output, makes an adverse effect on speed estimation. More specifically, it causes oscillatory ripples in the estimated parameters. For example, an h-order harmonic component can lead to an (h-1)-order harmonic ripple appearing in the estimated parameters [92]–[95]. In addition, the dc offsets lead to low-order disturbances in the estimated quantities, and even a narrow-bandwidth estimation scheme cannot successfully eliminate these low-order disturbances [96]–[98]. Another challenge to speed estimation is the issue of parameter variations, which is regarded as a tricky problem that may degrade estimation performance and even aggravate system instability [12]–[18]. Therefore, disturbance attenuation is desirable to be developed in the PLL- and FLL-based schemes.

Fig. 18 shows the implementation of the PLL- and FLL-based schemes with disturbance attenuation, which consists of four parts: a rotor back electromotive force signals (EMFs) or rotor flux observer, two adaptive filters, an AN unit, and the PLL- and FLL-based schemes. According to the stator voltage and stator current signals, the observer provides the estimated rotor back EMFs or the estimated rotor flux, as the inputs of the PLL- and FLL-based schemes. Afterward, the adaptive filters are employed to mitigate harmonics in the estimated rotor back EMFs or the estimated rotor flux. After the AN stage, the estimated speed and phase are obtained from the PLL- and FLL-based schemes. Generally, the estimated phase is fed back to the control system, as the rotor flux orientation phase. Eventually, the estimated rotor speed is obtained as

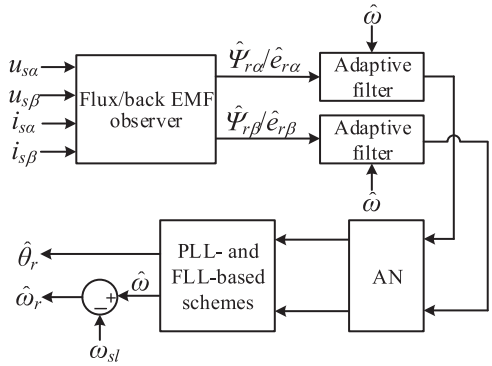

Fig. 18. Block diagram of the practical implementation of the PLL- and FLL-based schemes with disturbance attenuations.

$$\hat{\omega}_r = \hat{\omega} - \omega_{sl}. \tag{46}$$

It is interesting to mention that, in the PLL schemes, the adaptive filters can be plugged in the main feedback loop as in-loop filters; or, the filters can also be placed before the inputs as prefilters (see Fig. 18). Compared to the in-loop filters, the pre-filters have less adverse effects on the dynamic behavior of the PLL-based schemes [99], [100]. Hence, the prefilters are focused in this article.

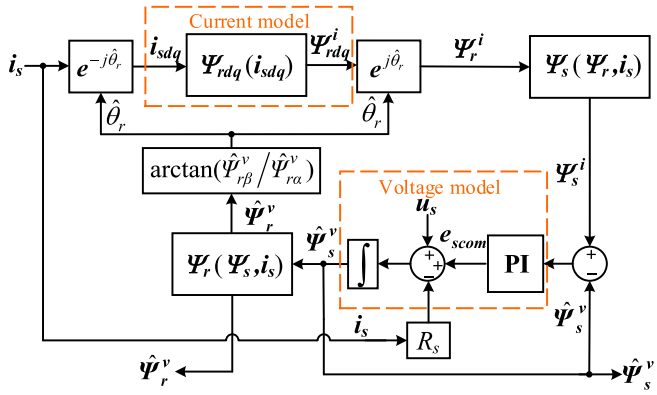

Fig. 19. Block diagram of the CLFO, in which a compensation unit is used to deal with dc offsets.

Clearly, the performance of the observers and the adaptive filters will affect the entire estimation performance, as detailed in the following.

B. Observers With DC Offset Mitigation

Both the PLL- and FLL-based schemes are vulnerable to the dc offsets in their inputs. This is because even a small dc drift may result in large ripples in the estimated parameters. It is known that the inputs of the PLL- and FLL-based schemes are the rotor back EMFs or the rotor flux. Hence, a straightforward solution is to use the high-performance observers that can eliminate dc offsets. Indeed, various observers have been reported in the literature to improve the immunity to dc offsets. Four are exemplified in the following.

The closed-loop flux observer (CLFO) is a promising candidate in terms of satisfactory estimation and adequate robustness against dc offsets, which is illustrated in Fig. 19. As shown, the CLFO is an adaptive combination of two common flux observers [i.e., the voltage model (VM) and the current model (CM) based flux observers].The two open-loop flux observers (i.e., VM- and CM-based flux observers) are regulated together by a PI controller. Notice that, the compensation signals, which are used in the VM-based flux observer, are provided from this PI controller. By doing so, the CLFO is expected to tackle the challenge of dc offsets [101], [102]. Moreover, the CLFO can be further extended as a full-order observer by using the sliding mode (SM) method (referred to as the FSMO) [103]–[105], which is presented in Fig. 20. As shown, in the FSMO, both the stator current and the flux signals are estimated simultaneously in this observer, while only the flux signals are estimated in the CLFO. Due to the use of the SM method, the robustness of the FSMO is further improved at the cost of tough parameter tuning and potential chatting behavior.

An interesting approach is to use the SOGI-QSGs as the flux observer. According to the presentation of the SOGI-QSG in Fig. 3(a), the transfer functions of the SOGI-QSG can be expressed as

$$D(s) = \frac{\hat{v}(s)}{v(s)} = \frac{k\hat{\omega}s}{s^2 + k\hat{\omega}s + \hat{\omega}^2} \tag{47}$$

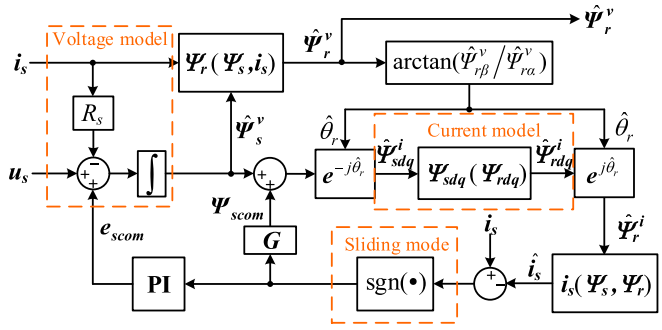

Fig. 20. Block diagram of the full-order observer with the SM method, which is regarded as an extension of the CLFO.

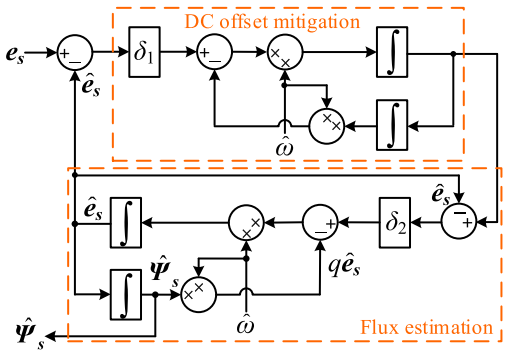

Fig. 21. Block diagram of the second-order SOGI flux observer, in which a SOGI-QSG is adopted as prefilter for dc offset elimination.

$$Q(s) = \frac{q\hat{v}(s)}{v(s)} = \frac{k\hat{\omega}^2}{s^2 + k\hat{\omega}s + \hat{\omega}^2} \tag{48}$$

where the outputs $\hat{v}$ and $q\hat{v}$ are regarded as the band-pass-filtered signal and the low-pass-filtered signal of the inputs, respectively [62]–[67]. More specifically, by substituting $s = j\omega$, the amplitude-frequency characteristics of $D(s)$ and $Q(s)$ can be written as

$$|D(j\omega)| = \left|\frac{jk\hat{\omega}\omega}{\hat{\omega}^2 - \omega^2 + jk\hat{\omega}\omega}\right| = \frac{k\hat{\omega}\omega}{\sqrt{(\hat{\omega}^2 - \omega^2)^2 + (k\hat{\omega}\omega)^2}} \tag{49}$$

$$|Q(j\omega)| = \left|\frac{k\hat{\omega}^2}{\hat{\omega}^2 - \omega^2 + jk\hat{\omega}\omega}\right| = \frac{k\hat{\omega}^2}{\sqrt{(\hat{\omega}^2 - \omega^2)^2 + (k\hat{\omega}\omega)^2}} \tag{50}$$

which suggests that the amplitude will be zero when the dc components pass through $D(s)$. Regrading $q\hat{v}$, it may not have the feature that can successfully attenuate the dc components. Notice that the signal of $q\hat{v}$ should be fed back to involve the flux estimation. Therefore, the flux observation is still deteriorated due to dc offsets. Considering the dc offset filtering capability of the input $\hat{v}$ is benefiting from $D(s)$, the robustness of the flux observer against dc offsets can be obtained by using the pre-filter whose transfer function is like $D(s)$ [106], [107]. As a consequence, this kind of flux observer (referred to as the second-order SOGI flux observer) is depicted in Fig. 21, in which δ_1 and δ_2 are the gains of the second-order SOGI flux

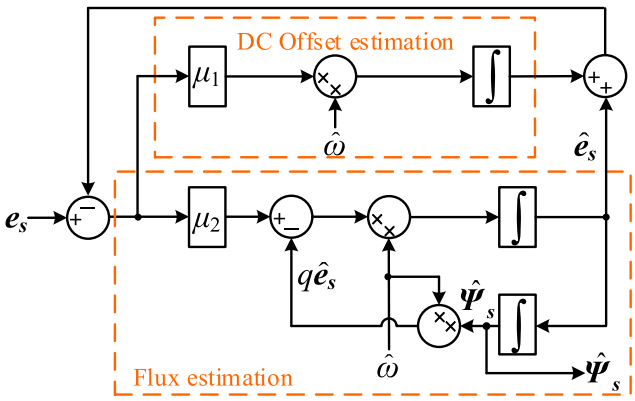

Fig. 22. Block diagram of the first-order SOGI flux observer, in which an extra loop is used for dc offset estimation.

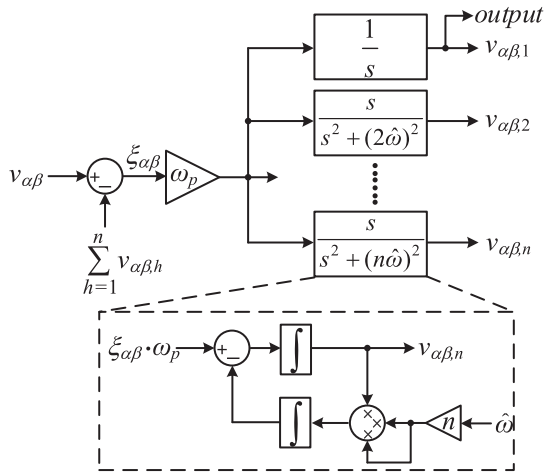

Fig. 23. Block diagram of the MSHF, in which ω_p is the gain of the MSHF.

observer. An alternative approach to support the SOGI-based flux observer mitigate the dc offsets is to employ a first-order SOGI flux observer, as presented in Fig. 22 (in which μ_1 and μ_2 are the gains of the first-order SOGI flux observer) [108], [109]. This flux observer introduces a loop that can estimate the dc offset effectively, and then, the estimated dc offset is subtracted from the inputs. By doing so, the dc offsets in estimated flux are effectively mitigated. Different from the flux observers shown in Figs. 19 and 20, the estimated speed should be fed back into the two observers, and accordingly, the second-order SOGI flux observer and the first-order SOGI flux observer are identified as speed-adaptive observers.

Compared to the first-order SOGI flux observer, the second-order SOGI flux observer needs similar parameter tuning efforts and implementation complexity but has better filtering characteristics due to its higher attenuation capability. Therefore, as a dc offset mitigation unit, the second-order SOGI flux observer is preferable. However, the estimated speed should be fed back into these two observers, which may lead to certain issues. That is, an inaccurate speed estimation has an obvious impact on flux observation. In turn, the improper estimated flux may further exacerbate speed estimation. This may also appear in the first-order SOGI flux observer. Moreover, the SOGI-based flux observers may suffer from delay effects and noise due to the feedback of estimated speed. By comparison, the CLFO and the FSMO (these observers are generally named as the inherently sensorless flux observers) make a considerable performance improvement. It can be observed that the estimated speed feedback is cancelled in these observers. With this, the undesirable impact caused by the speed feedback is effectively suppressed. Main concerns of the inherently sensorless flux observers are difficult implementation and more control parameters. That means, more computational efforts and tougher parameter tuning are required in these observers, compared to the SOGI-based flux observers.

C. Adaptive Filters

In induction motor drives, harmonics are mainly attributable to the inverter nonlinear output. This situation becomes serious in high-power applications, e.g., high-speed railway traction drives, metro traction drives, etc. In these applications, to ensure low switching losses, the switching frequency should be low (generally, less than 1 kHz). As a result, abundant harmonics appear in motor drives. Additionally, the arctangent and differential operations will further enlarge harmonic impact. The harmonics, as mentioned before, causes considerable ripples that degrade estimation accuracy. Various adaptive filters have been recommended to mitigate harmonics in estimation schemes [110]–[113].

The multiple selective harmonic filter (MSHF) has been proven to be an effective harmonic suppression method [110], and the block diagram of this filter is shown in Fig. 23. The MSHF is composed of several units, and these units are arranged in parallel, working in a collaborative way. Each unit of the MSHF can be taken as a filter that is responsible for extracting a selective harmonic component from the inputs. Then, the selected harmonic components are subtracted from the inputs. In this case, the effects of harmonics are effectively reduced. Notice that, to deal with the issue of frequency variations, the estimated speed is fed back to the structure of the MSHF. This harmonic filtering method can be extended to the multiple adaptive vector filter (MAVF) [111], which is presented in Fig. 24. The major difference between the MSHF and the MAVF is the sub-structure of the two adaptive filters.

Considering the band-pass filter characteristic of the SOGI-QSG in the SOGI-FLL scheme, the task of selective harmonic elimination can also be carried out by the multiple SOGI-based adaptive filter (MSOGI-AF) [114]–[117], which is illustrated in Fig. 25. As shown, this filter consists of a set of SOGI-QSGs in order to extract the frequency components of interest from the inputs simultaneously. Another attempt to enhance harmonic suppression capability of the speed estimation schemes by using the multiple ROGI-based adaptive filter (MROGI-AF) is made [118], as depicted in Fig. 26. As shown, the resultant filter structure is the same as the MSOGI-AF except that the SOGI-QSGs are replaced with the ROGI-based units.

By analyzing the structures of these adaptive filters, it can be seen that the main difference is its substructure. In particular, the strong coupling can be observed in the MAVF and the MROGI-AF, while the MSHF and the MSOGI-AF are free from

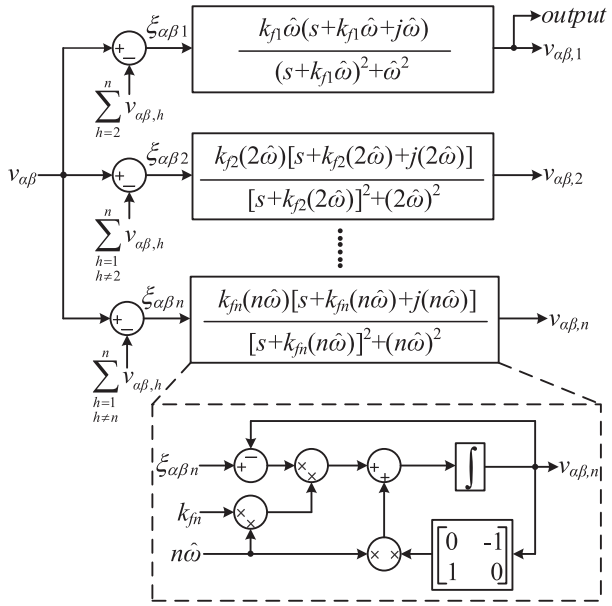

Fig. 24. Block diagram of the MAVF, in which k_{fn} is the gain of the MAVF.

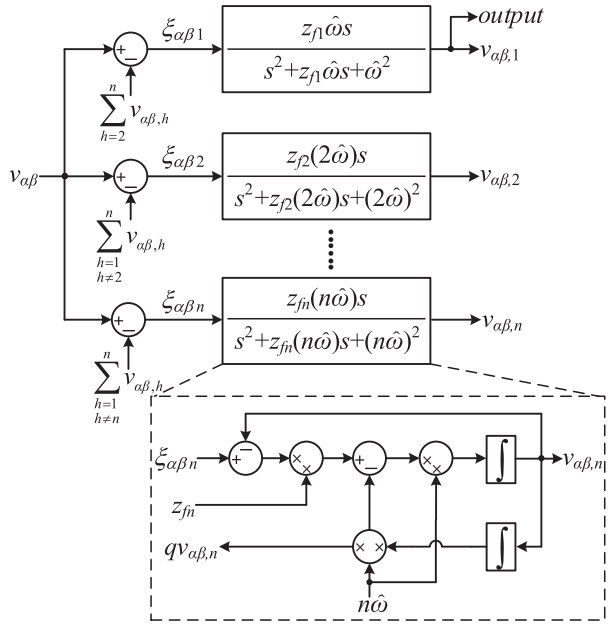

Fig. 25. Block diagram of the MSOGI-AF, in which z_{fn} is the gain of the MSOGI-AF.

this coupling. Moreover, a group of units operate in a cooperative manner in these filters, each of which aims at extracting a specific harmonic component. It is worth noting that the adaptive filters need more computational efforts when more harmonic filtering units involve in the filter. Therefore, a tradeoff between computational burden and harmonic filtering performance should be deliberately made. In addition, the speed information is used as an adaptive quantity in the filters, which means that these filters may suffer from unexpected effects. For example, since the speed estimation is the last step of the entire estimation scheme, the adaptive filters may experience time delays and noise due to

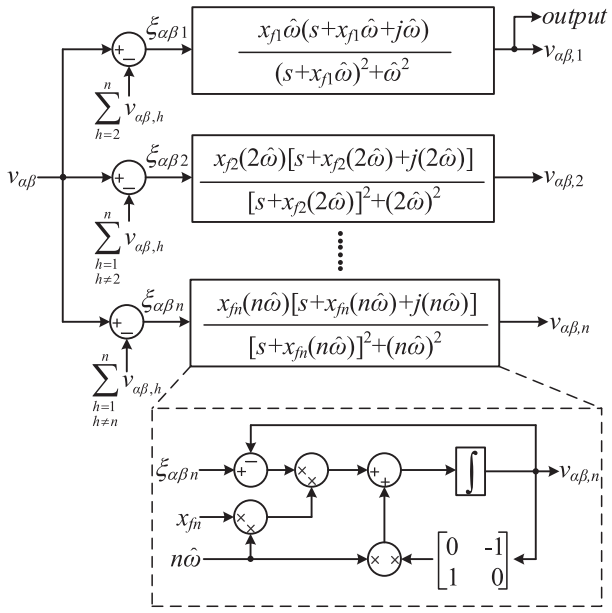

Fig. 26. Block diagram of the MROGI-AF, in which x_{fn} is the gain of the MROGI-AF.

speed feedback. Moreover, the incorrect speed information may further degrade the performance of the adaptive filters.

It is believed that there are still various adaptive filters that have not been covered in this article, such as the recursive-least-square-based adaptive filter [49], the multiple adaptive notch filter [50], the adaptive linear neural network-based filter [52], and the multiple complex vector filter [111]–[113], etc. These nonappearing adaptive filters can be seen as the extensions or relatives of the abovementioned adaptive filters.

D. Parameter Estimation Schemes

In the model-based speed estimation schemes, e.g., PLL- and FLL-based schemes, the involvement of motor parameters may become a challenge when considering parameter variations. This is particularly true when stator resistance variations are seen in induction motor drives due to temperature rise, skin effect, etc. The stator resistance variations contribute to performance degradation and even increase the risk of system instability. Regarding the potential solutions to parameter variations, typically, it is implemented through various parameter online estimation schemes.

In the PLL- and FLL-based schemes, the issue of parameter variations will affect the estimated rotor back EMFs or the estimated rotor flux, i.e., the inputs of the estimation schemes. Taking the PLL scheme as an example, the effect of parameter variations on estimation performance is analyzed as follows. Supposing the inputs of the PLL scheme without parameter variations are sinusoidal, as

$$\begin{cases} v_\alpha = V\cos\theta \\ v_\beta = V\sin\theta \end{cases}. \tag{51}$$

Then, it can be obtained that

$$\begin{cases} v_d = V\cos(\theta - \hat{\theta}) \\ v_q = V\sin(\theta - \hat{\theta}) \end{cases}. \tag{52}$$

Accordingly, the inputs of the PLL scheme considering parameter variations can be obtained as

$$\begin{cases} v_{\alpha d} = (V + \Delta V)\cos(\theta + \Delta\theta) \\ v_{\beta d} = (V + \Delta V)\sin(\theta + \Delta\theta) \end{cases} \tag{53}$$

with ΔV and $\Delta\theta$ being the amplitude deviation and the phase deviation caused by parameter variations. Subsequently,

$$\begin{cases} v_{dd} = (V + \Delta V)\cos(\theta + \Delta\theta - \hat{\theta}) \\ v_{qd} = (V + \Delta V)\sin(\theta + \Delta\theta - \hat{\theta}) \end{cases} \tag{54}$$

which can be expanded as

$$\begin{aligned} v_{dd} &= (V + \Delta V)\cos(\theta - \hat{\theta})\cos(\Delta\theta) \\ &\quad - (V + \Delta V)\sin(\theta - \hat{\theta})\sin(\Delta\theta) \\ &= \underbrace{V\cos(\theta - \hat{\theta})}_{v_d} + D_d \end{aligned} \tag{55}$$

$$\begin{aligned} v_{qd} &= (V + \Delta V)\sin(\theta - \hat{\theta})\cos(\Delta\theta) \\ &\quad + (V + \Delta V)\cos(\theta - \hat{\theta})\sin(\Delta\theta) \\ &= \underbrace{V\sin(\theta - \hat{\theta})}_{v_q} + D_q \end{aligned} \tag{56}$$

in which D_d and D_q are the disturbance terms caused by parameter variations, respectively. Based on (55) and (56), it can be deduced that

$$\hat{\theta}_d = \underbrace{\frac{Vk_ps + Vk_i}{s^2 + Vk_ps + Vk_i}\theta}_{\hat{\theta}} + \frac{k_ps + k_i}{s^2 + Vk_ps + Vk_i}D_q \tag{57}$$

$$\hat{\omega}_d = \underbrace{\frac{Vk_ps + Vk_i}{s^2 + Vk_ps + Vk_i}\omega}_{\hat{\omega}} + \frac{s(k_ps + k_i)}{s^2 + Vk_ps + Vk_i}D_q \tag{58}$$

where $\hat{\theta}_d$,$\hat{\theta}$, $\hat{\omega}_d$, and $\hat{\omega}$ are the estimated phase with parameter variations and without parameter variations, the estimated frequency with parameter variations and without parameter variations. According to (57) and (58), when considering parameter variations, the estimated frequency and the estimated phase suffer from the disturbance term of D_q. Therefore, in order to guarantee estimation performance, parameter estimation schemes are necessary, when considering the disturbance of parameter variations.

Among various motor parameters, stator resistance variations should be specifically considered. Hence, many stator resistance estimation methods, including the MRAS [15], [26]–[30], the EKF [22], [23], and the ANN [41], have been developed in the literature. Schemes using the MRAS methods are of interest, due to being simple and providing satisfactory performance. Here, a simple yet effective example of the MRAS-type stator resistance estimation schemes is presented in Fig. 27. As shown in Fig. 27, in this scheme, the CM-based flux observer is used as the reference model while the VM-based flux observer acts as the adaptive model. A PI controller is adopted to achieve stator resistance estimation, and consequently, the estimated stator resistance is fed back to the VM-based flux observer to guarantee speed estimation. Furthermore, the estimated rotor resistance is then obtained by considering the same thermal behavior for stator and rotor resistances [103].

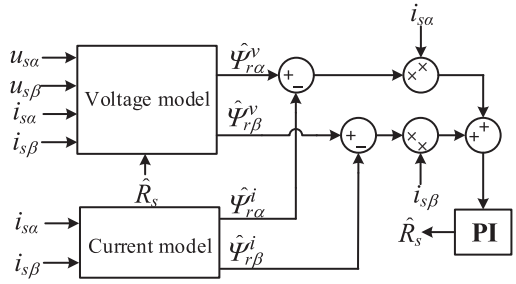

Fig. 27. Block diagram of a typical MRAS-type scheme for stator resistance estimation.

TABLE II
PARAMETERS OF THE INDUCTION MOTOR DRIVES

Parameter	Value	Parameter	Value
Rated Power (kW)	2.2	Stator resistance (Ω)	3.67
Rated voltage (V)	220	Rotor resistance (Ω)	2.32
Rated current (A)	5.1	Stator inductance (mH)	244.2
Rated speed (r/min)	1430	Rotor inductance (mH)	247.3
Pole pairs	2	Magnetizing inductance (mH)	235

Notably, a compensation unit in the CLFO can successfully deal with various errors, such as dc offsets and stator resistance variations. Accordingly, this flux observer can handle the issue of stator resistance variations [101]–[103].

VII. CASE STUDIES

In this section, case studies are performed to verify the aforementioned discussions through experimental tests, in which the performance of two representative schemes is investigated. The experimental tests are performed referring to the block diagram of the entire speed-sensorless-controlled induction motor drive system in Fig. 28. The experiment set-up is presented in Fig. 29, which consists of an inverter (Danfoss FC302), a 2.2-kW induction motor (ABB M2T100LA28-4 MK110022-S), a mechanically coupled load surface-mounted permanent-magnet synchronous motor (Siemens 1FT6084-8SH71-1AAC), and a dSPACE 1103 control platform. The parameters of the induction motor drives are given in Table II.

A. Performance of the SOGI-RFLL Scheme Under Speed Command Variations

The estimation performance of the SOGI-RFLL scheme under speed command variations is shown in Fig. 30. In this case, the speed command is varied from 1000 to 1430 r/min (rated speed), and then back to 1200 r/min. And, the load in this case is

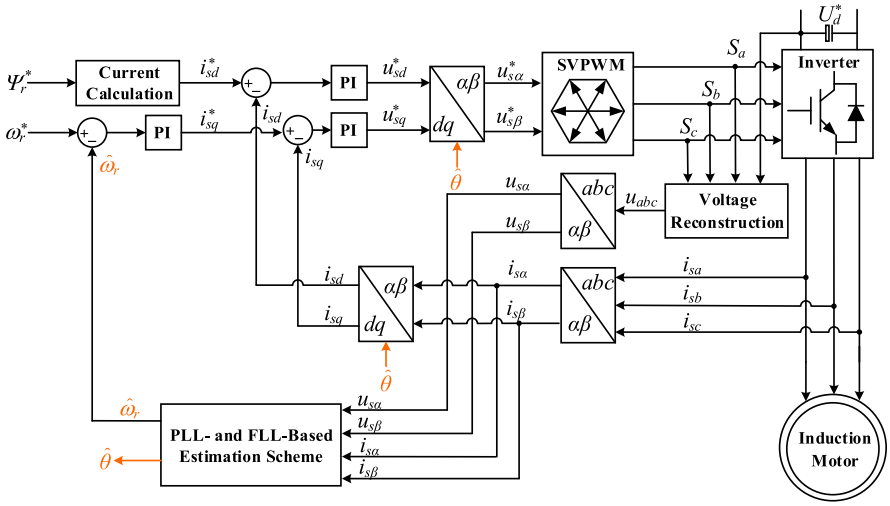

Fig. 28. Block diagram of the speed-sensorless-controlled induction motor drive system (SVPWM-Space vector pulse-width modulation).

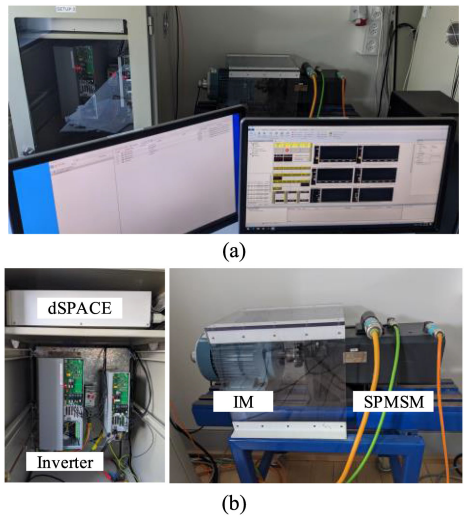

(a)

(b)

Fig. 29. Experimental set-up system. (a) Entire induction motor drives. (b) Inverter and induction motor drives.

7 N·m (50% rated load). From the test results, it can be observed that the satisfactory performance is achieved in terms of speed estimation by using the SOGI-RFLL scheme. Meanwhile, the estimation error is within a reasonable range. The performance of the conventional SOGI-FLL scheme is also provided as a comparison, which is presented in Fig. 31. In the SOGI-FLL scheme, the test case is the same to that in the SOGI-RFLL scheme. As shown in Fig. 31, a compromised estimation accuracy is achieved by using the SOGI-FLL scheme. That is, obvious estimation errors are observed during acceleration and deceleration processes, which may become a problem in the applications that require induction motor to frequently work in acceleration and deceleration processes. The phase estimation performance of the two schemes is presented in Figs. 32 and 33, respectively. According to the test results in Fig. 32, it is indicated that the estimated phase of the SOGI-RFLL scheme works well.

B. Performance of the ROGI-RFLL Scheme Under Speed Command Variations

The performance of the ROGI-RFLL scheme is also evaluated, and compared to that of the conventional ROGI-FLL scheme. The test cases are identical to those in the SOGI-FLL scheme and the SOGI-RFLL scheme. According to the results shown in Fig. 34, the ROGI-RFLL scheme behaves well in this case, and accordingly, the estimation error is acceptable. By comparison, as shown in Fig. 35, the presence of apparent estimation errors makes performance degradation on the conventional ROGI-FLL scheme during acceleration and deceleration processes. The phase estimations provided by the ROGI-RFLL scheme and the ROGI-FLL scheme are shown in Figs. 36 and 37, respectively. As seen in Fig. 36, the phase estimation performance of the ROGI-RFLL scheme is acceptable in the entire speed range.

In all, seen from the experimental results, it is indicated that the conventional SOGI-FLL scheme and the conventional ROGI-FLL scheme suffer from performance degradation during acceleration and deceleration processes. Both the SOGI-RFLL scheme and the ROGI-RFLL scheme, nevertheless, can provide speed estimation with a satisfactory accuracy in this circumstance. Comparisons between the RFLL schemes and the conventional FLL schemes suggest that the RFLL schemes are better options in terms of estimation accuracy, when being applied in induction motor drives.

C. Performance of the Adaptive Filters

The performance of adaptive filters in different estimation schemes is explored, and the results are shown in Figs. 38 and 39, respectively. In the two cases, the speed command and load are set to 1430 r/min (rated speed) and 7 N·m (50% rated load), respectively.

As shown in Fig. 38, when the adaptive filters are absent in the PLL scheme, the estimated rotor flux (as the inputs of the PLL scheme) is distorted, and then, the ripples appear in the estimated phase. By comparison, when enabling the adaptive

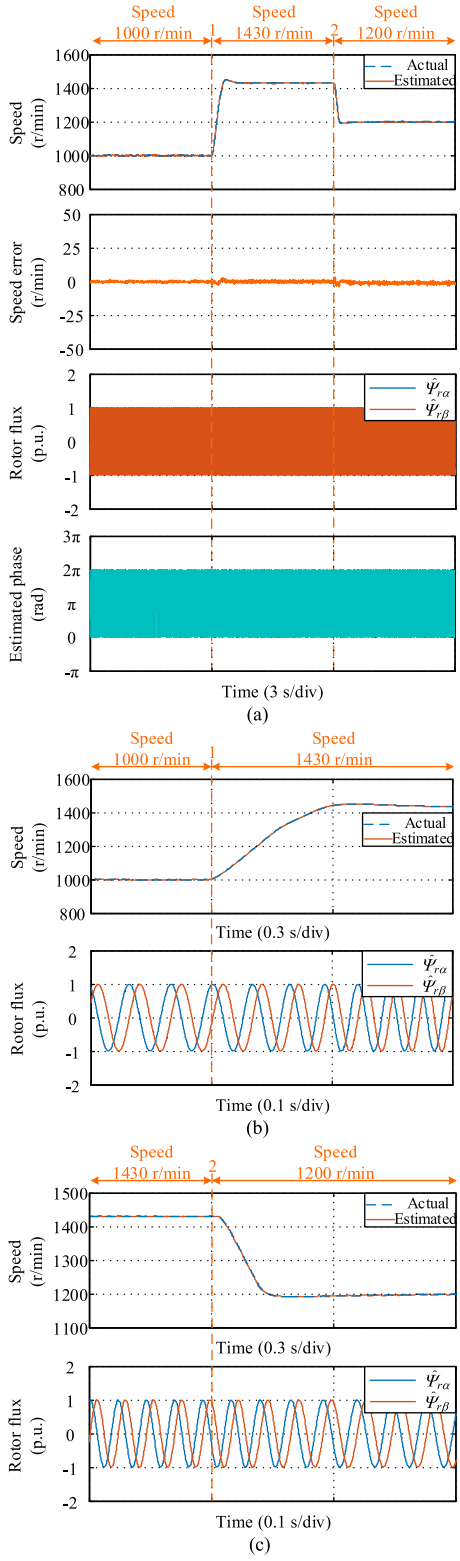

Fig. 30. Estimation performance of the SOGI-RFLL scheme under speed command variations. (a) Entire estimation performance. (b) Zoom-in 1. (c) Zoom-in 2.

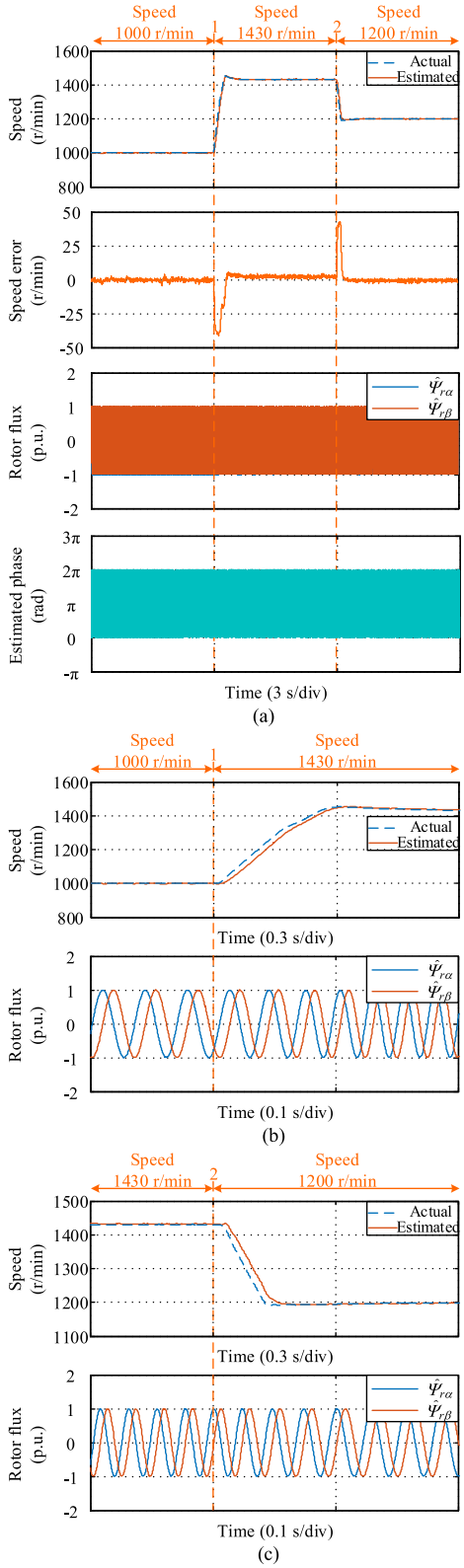

Fig. 31. Estimation performance of the conventional SOGI-FLL scheme under speed command variations. (a) Entire estimation performance. (b) Zoom-in 1 (c) Zoom-in 2.

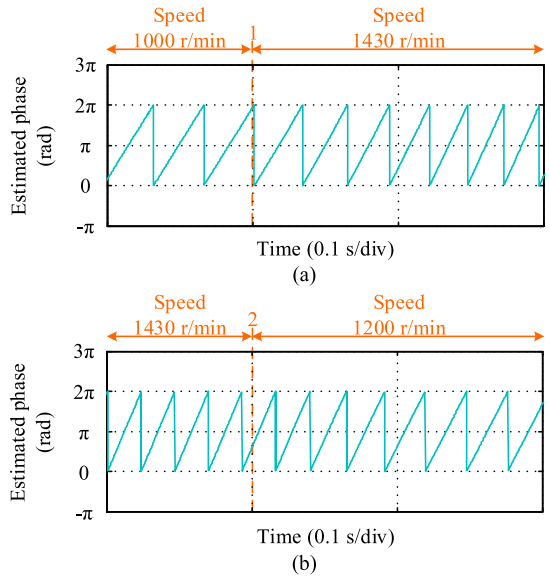

Fig. 32. Estimation performance of the rotor flux phase by using the SOGI-RFLL scheme under speed command variations. (a) Zoom-in 1 of Fig. 30. (b) Zoom-in 2 of Fig. 30.

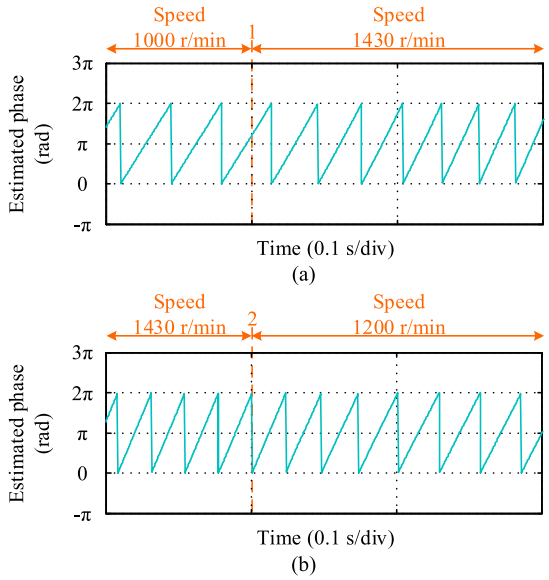

Fig. 33. Estimation performance of the rotor flux phase by using the conventional SOGI-FLL scheme under speed command variations. (a) Zoom-in 1 of Fig. 31. (b) Zoom-in 2 of Fig. 31.

filters, the distortions in the estimated rotor flux are obviously alleviated. Consequently, the phase estimation is ensured. The situation still occurs in the SOGI-RFLL scheme, as shown in Fig. 39. From the test results, it is clear that with the assistance of the adaptive filters, the SOGI-RFLL scheme can maintain speed and phase estimations.

D. Performance of the Rotor Back EMFs

The performance of the rotor back EMFs with different conditions is experimentally tested, and the corresponding results

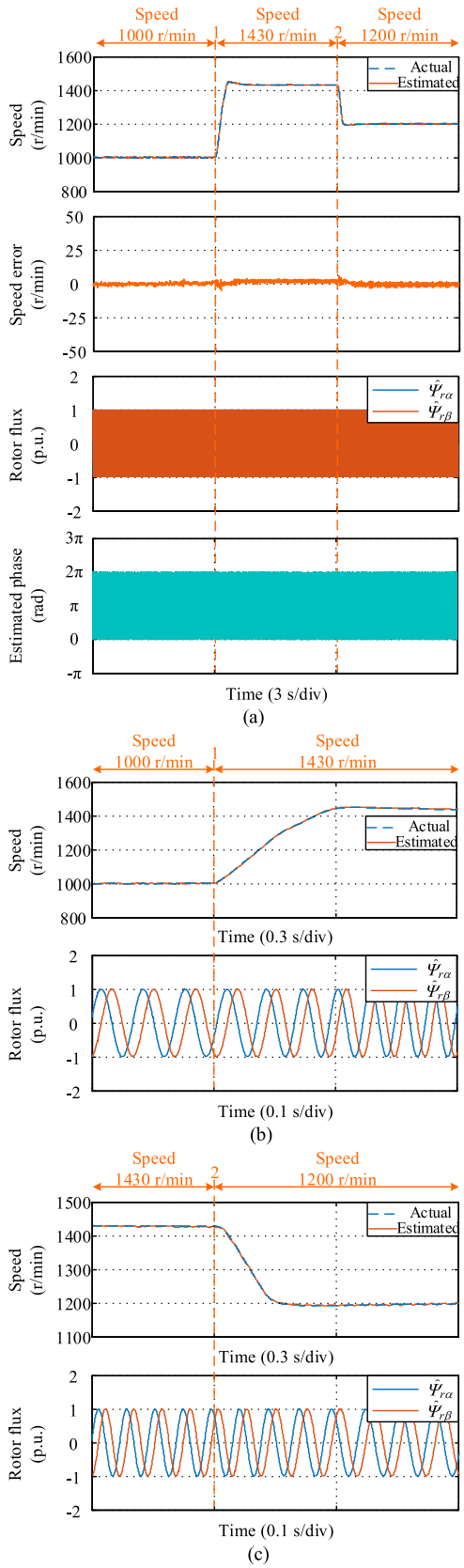

Fig. 34. Estimation performance of the ROGI-RFLL scheme under speed command variations. (a) Entire estimation performance. (b) Zoom-in 1. (c) Zoom-in 2.

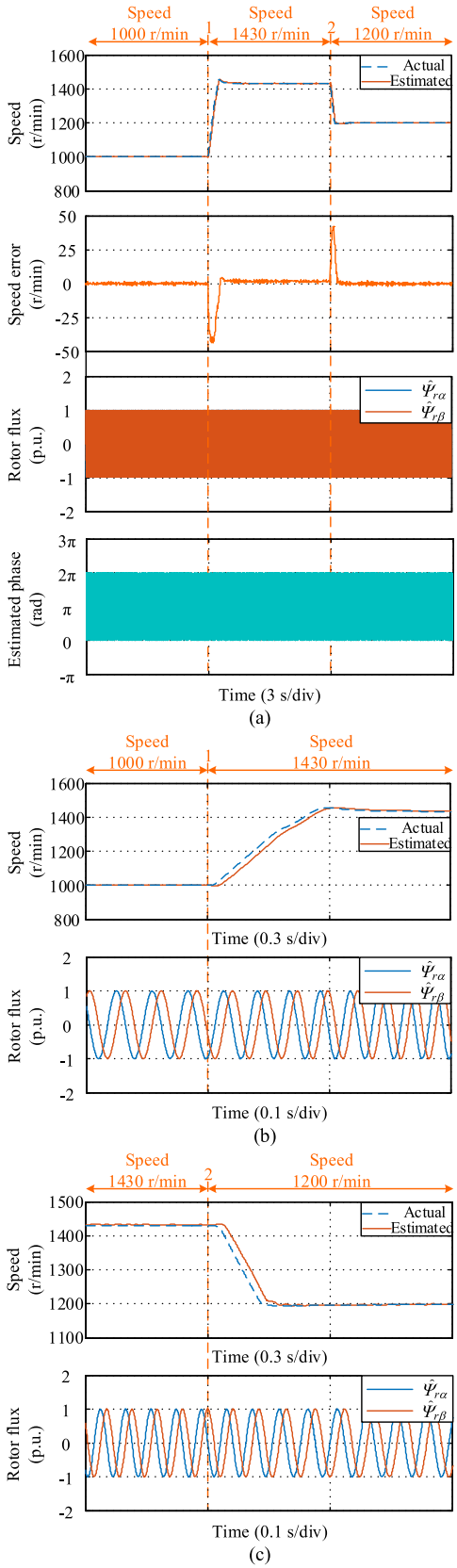

Fig. 35. Estimation performance of the conventional ROGI-FLL scheme under speed command variations. (a) Entire estimation performance. (b) Zoom-in 1. (c) Zoom-in 2.

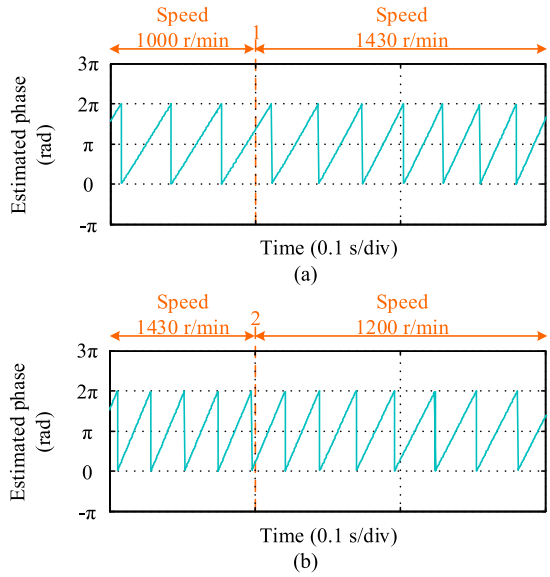

Fig. 36. Estimation performance of the rotor flux phase by using the ROGI-RFLL scheme under speed command variations. (a) Zoom-in 1 of Fig. 34. (b) Zoom-in 2 of Fig. 34.

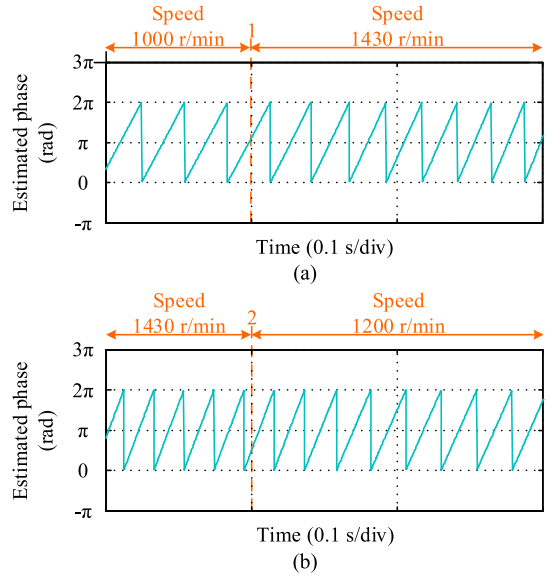

Fig. 37. Estimation performance of the rotor flux phase by using the conventional ROGI-FLL scheme under speed command variations. (a) Zoom-in 1 of Fig. 35. (b) Zoom-in 2 of Fig. 35.

are given in Table III (to reduce manuscript-page). As given in Table III, when the proposed FLL scheme works in the high-speed range, a larger load makes more distortions appear in the rotor back EMFs. Additionally, it is known that with the increase of the load, distortions in the rotor back EMFs become obvious when the proposed SOGI-RFLL scheme operates in the low-speed range. This issue can be attributed to the increasing inductance saturation with the increased load.

Moreover, observations in Table III indicate that when the proposed SOGI-RFLL scheme operates in the low-speed range, the rotor back EMFs contain undesirable distortions. By contrast,

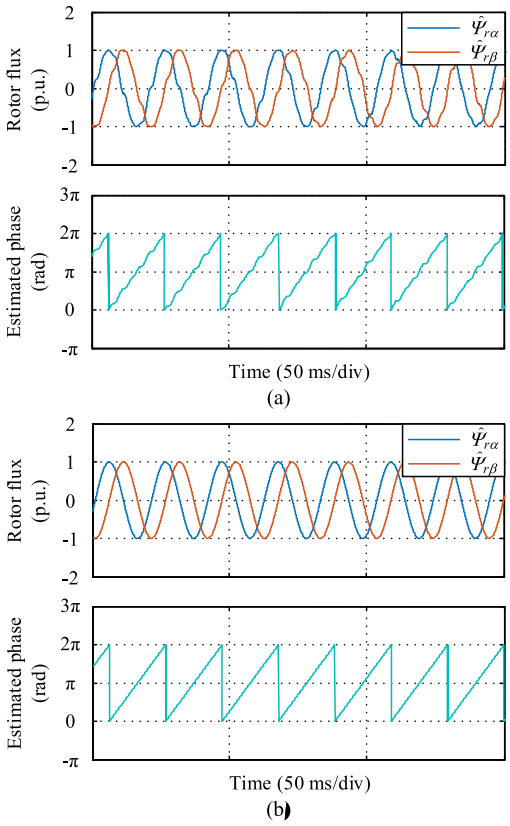

Fig. 38. Estimation performance of the rotor flux phase using the PLL scheme under harmonics. (a) Without adaptive filters. (b) With adaptive filters.

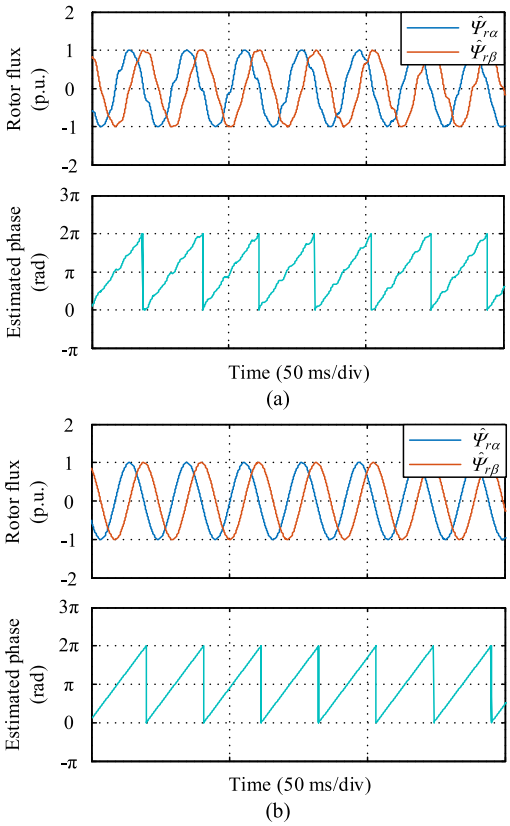

Fig. 39. Estimation performance of the rotor flux phase using the SOGI-RFLL under harmonics. (a) Without adaptive filters. (b) With adaptive filters.

TABLE III
PERFORMANCE OF THE ROTOR BACK EMFS WITH DIFFERENT CASES

Test Case		Total Harmonic Distortion (THD)
Speed (r/min)	Load (N•m)	
1200	25% rated load	1.10%
	50% rated load	3.03%
	75% rated load	7.19%
150	25% rated load	13.11%
	50% rated load	21.30%
	75% rated load	41.01%

the impact of distortions on the rotor back EMFs is minimized when the proposed SOGI-RFLL scheme operates in the high-speed range. When a heavy load, i.e., 75% rated load, is applied in the proposed SOGI-RFLL scheme, the same conclusion can be drawn. That is, a higher speed leads to smaller distortions in the rotor back EMFs.

VIII. CONCLUSION

This article has discussed different PLL- and FLL-based schemes for speed estimation. Specifically, a performance investigation of the state-of-the-art PLL-based schemes together with new attempts of the FLL-based schemes was presented to indicate the development of solutions toward the challenge of frequency ramps. It has been revealed that the increased-order PLL schemes, including the type-3 PLL schemes and the dual-loop PLL schemes, are effective in tackling the frequency ramp issue at the cost of dynamic performance and stability margin. This situation still occurs in the EFLL-based schemes, e.g., the SOGI-EFLL scheme and the ROGI-EFLL scheme. In addition, the RFLL schemes, e.g., the SOGI-RFLL scheme and the ROGI-RFLL scheme, are recommended because these schemes achieve accurate estimation by employing the new-type FLL units, rather than solely increasing the system order or introducing the extra compensation units. Thus, system dynamics and stability margin are maintained.

Moreover, disturbances in motor drives, e.g., dc offset, harmonics, and parameter variations, will challenge the performance in speed estimation. Various disturbance elimination schemes were detailed in the implementation of the PLL- and FLL-based schemes, notable examples of which have also been highlighted. Case studies were provided to evaluate the estimation performance of two representative schemes, i.e., the SOGI-RFLL scheme and the ROGI-RFLL scheme.

From this article, it can be concluded that the following.

1) Although the increased-order PLL schemes and the EFLL schemes show good estimation performance under acceleration and deceleration cases, several issues, e.g., low stability margin and poor system dynamics, remain to be resolved.
2) The RFLL schemes, including the SOGI-RFLL scheme and the ROGI-RFLL scheme, are promising candidates in terms of estimation accuracy and stability margin. However, further efforts should be made to handle the issue of frequency feedback in the two schemes.

3) As seen, the RFLL schemes mostly work in the stationary reference frame. Due to this, it is highly difficult to establish accurate small-signal models of these schemes. Therefore, the stability analysis and parameter tuning of the RFLL schemes should take more considerations.
4) Though adaptive filters can effectively suppress harmonics when considering the presence of abundant harmonics, they also lead to issues like heavy computational burden and discretization complexity. Moreover, another concern in the adaptive filters is the feedback of estimated speed. With this, issues of huge delays and undesired noise need to be further resolved.
5) The robustness against parameter variations can be obtained through parameter estimation schemes. This, however, may increase system complexity and computational burden. A tradeoff between the implementation complexity and estimation performance should be made.
6) With certain proper adjustments, these PLL- and FLL-based schemes can be further extended to other motor drive systems for dealing with the frequency ramps issue, e.g., for synchronous motors, brushless dc motors, synchronous generators, etc.

REFERENCES

[1] J. Holtz, "Sensorless position control of induction motors—An emerging technology," *IEEE Trans. Ind. Electron.*, vol. 45, no. 6, pp. 840–851, Dec. 1998.

[2] J. Holtz, "Sensorless control of induction motor drives," *Proc. IEEE*, vol. 90, no. 8, pp. 1359–1394, Aug. 2002.

[3] J. Holtz, "Sensorless control of induction machine—With or without signal injection?", *IEEE Trans. Ind. Electron.*, vol. 53, no. 1, pp. 7–30, Feb. 2006.

[4] C. Caruana, G. M. Ashe, and M. Sumner, "Performance of HF signal injection techniques for zero-low-frequency vector control of induction machines under sensorless conditions," *IEEE Trans. Ind. Electron.*, vol. 53, no. 1, pp. 225–238, Feb. 2006.

[5] V. M. Leppanen and J. Luomi, "Observer using low-frequency injection for sensorless induction motor control—Parameter sensitivity analysis," *IEEE Trans. Ind. Electron.*, vol. 53, no. 1, pp. 216–224, Feb. 2006.

[6] Q. Gao, G. Asher, and M. Sumner, "Sensorless position and speed control of induction motors using high-frequency injection and without offline precommissioning," *IEEE Trans. Ind. Electron.*, vol. 54, no. 5, pp. 2474–2481, Oct. 2007.

[7] A. Consoli, G. Scarcella, G. Scelba, S. Royak, and M. M. Harbaugh, "Implementation issues in voltage zero sequence-based encoderless techniques," *IEEE Trans. Ind. Appl.*, vol. 44, no. 1, pp. 144–152, Jan./Feb. 2008.

[8] R. Raute, C. Caruana, C. S. Staines, J. Cilia, M. Sumner, and G. M. Asher, "Sensorless control of induction machines at low and zero speed by using PWM harmonics for rotor-bar slotting detection," *IEEE Trans. Ind. Appl.*, vol. 46, no. 5, pp. 1989–1998, Sep./Oct. 2010.

[9] Z. Gao, L. Turner, R. S. Colby, and B. Leprettre, "A frequency demodulation approach to induction motor speed detection," *IEEE Trans. Ind. Appl.*, vol. 47, no. 4, pp. 1632–1642, Jul./Aug. 2011.

[10] L. Zhao, J. Huang, J. Chen, and M. Ye, "A parallel speed and rotor time constant identification scheme for indirect field oriented induction motor drives," *IEEE Trans. Power Electron.*, vol. 31, no. 9, pp. 6494–6503, Sep. 2016.

[11] A. G. Yepes, J. D. Gandoy, F. Baneira, and H. A. Toliyat, "Speed estimation based on rotor slot harmonics in multiphase induction machines under open-phase fault," *IEEE Trans. Power Electron.*, vol. 33, no. 9, pp. 7980–7993, Sep. 2018.

[12] M. S. Zaky, "Stability analysis of speed and stator resistance estimators for sensorless induction motor drives," *IEEE Trans. Ind. Electron.*, vol. 59, no. 2, pp. 858–870, Jul. 2012.

[13] Z. Yin, Y. Zhang, C. Du, J. Liu, X. Sun, and Y. Zhong, "Research on anti-error performance of speed and flux estimation for induction motors based on robust adaptive state observer," *IEEE Trans. Ind. Electron.*, vol. 63, no. 6, pp. 3499–3510, Jun. 2016.

[14] J. Chen and J. Huang, "Globally stable speed-adaptive observer with auxiliary states for sensorless induction motor drives," *IEEE Trans. Power Electron.*, vol. 34, no. 1, pp. 33–39, Jan. 2019.

[15] J. Chen and J. Huang, "Stable simultaneous stator and rotor resistances identification for speed sensorless IM drives: Review and new results," *IEEE Trans. Power Electron.*, vol. 33, no. 10, pp. 8695–8709, Oct. 2018.

[16] J. Chen, J. Huang, and Y. Sun, "Resistances and speed estimation in sensorless induction motor drives using a model with known regressors," *IEEE Trans. Ind. Electron.*, vol. 66, no. 4, pp. 2659–2667, Apr. 2019.

[17] T. O. Kowalska, M. Korzonek, and G. Tarchala, "Stability improvement methods of the adaptive full-order observer for sensorless induction motor drive—Comparative study," *IEEE Trans. Ind. Informat.*, vol. 15, no. 11, pp. 6114–6126, Nov. 2019.

[18] J. Chen and J. Huang, "Alternative solution regarding problems of adaptive observer compensating parameters uncertainties for sensorless induction motor drives," *IEEE Trans. Ind. Electron.*, vol. 67, no. 7, pp. 5879–5888, Jul. 2020.

[19] M. Montanari, S. M. Peresada, C. Rossi, and A. Tilli, "Speed sensorless control of induction motors based on a reduced-order adaptive observer," *IEEE Trans. Control Syst. Technol.*, vol. 15, no. 6, pp. 1049–1064, Nov. 2007.

[20] M. Hinkkanen and L. Harnefors, "Complete stability of reduced-order and full-order observers for sensorless IM drives," *IEEE Trans. Ind. Electron.*, vol. 55, no. 5, pp. 1319–1329, Mar. 2008.

[21] M. Hinkkanen, L. Harnefors, and J. Luomi, "Reduced-order flux observers with stator-resistance adaptation for speed-sensorless induction motor drive," *IEEE Trans. Power Electron.*, vol. 25, no. 5, pp. 1173–1183, May 2010.

[22] M. Barut, S. Bogosyan, and M. Gokasan, "Experimental evaluation of braided EKF for sensorless control of induction motors," *IEEE Trans. Ind. Electron.*, vol. 55, no. 2, pp. 620–632, Feb. 2008.

[23] Z. Yin, G. Li, Y. Zhang, J. Liu, X. Sun, and Y. Zhong, "A speed and flux observer of induction motor based on extended Kalman filter and Markov chain," *IEEE Trans. Power Electron.*, vol. 32, no. 9, pp. 7096–7117, Sep. 2017.

[24] E. Zerdali and M. Barut, "The comparisons of optimized extended Kalman filters for speed-sensorless control of induction motors," *IEEE Trans. Ind. Electron.*, vol. 64, no. 6, pp. 4340–4351, Jun. 2017.

[25] M. Comanescu and L. Xu, "Sliding-mode MRAS speed estimators for sensorless vector control of induction machine," *IEEE Trans. Ind. Electron.*, vol. 53, no. 1, pp. 146–153, Feb. 2006.

[26] M. S. Zaky, M. M. Khater, S. S. Shokralla, and H. A. Yasin, "Wide-speed-range estimation with online parameter identification schemes of sensorless induction motor drives," *IEEE Trans. Ind. Electron.*, vol. 56, no. 5, pp. 1699–1707, May 2009.

[27] J. Chen and J. Huang, "Online decoupled stator and rotor resistances adaptation for speed sensorless induction motor drives by a time-division approach," *IEEE Trans. Power. Electron.*, vol. 32, no. 6, pp. 4587–4599, Jun. 2017.

[28] M. S. Zaky, M. K. Metwaly, H. Z. Azazi, and S. A. Deraz, "A new adaptive SMO for speed estimation of sensorless induction motor drives at zero and very low frequencies," *IEEE Trans. Ind. Electron.*, vol. 65, no. 9, pp. 6901–6911, Sep. 2018.

[29] H. Wang, X. Ge, and Y. C. Liu, "Second-order sliding-mode MRAS observer based sensorless vector control of linear induction motor drives for medium-low speed maglev applications," *IEEE Trans. Ind. Electron.*, vol. 65, no. 12, pp. 9938–9952, Dec. 2018.

[30] Y. Zhang, Z. Yin, Y. Zhang, J. Liu, and X. Tong, "A novel sliding mode observer with optimized constant rate reaching law for sensorless control of induction motor," *IEEE Trans. Ind. Electron.,* vol. 67, no. 7, pp. 5867–5878, Jul. 2020.

[31] T. O. Kowalska and M. Dybkowski, "Stator-current-based MRAS estimator for a wide range speed-sensorless induction-motor drive," *IEEE Trans. Ind. Electron.*, vol. 57, no. 4, pp. 1296–1308, Apr. 2010.

[32] M. Korzonek, G. Tarchala, and T. O. Kowalska, "A review on MRAS-type speed estimators for reliable and efficient induction motor drives," *ISA Trans.,* vol. 93, pp. 1–13, Oct. 2019.

[33] A. Teja, V. Verma, and C. Chakraborty, "A new formulation of reactive-power-based model reference adaptive system for sensorless induction motor drive," *IEEE Trans. Ind. Electron.*, vol. 62, no. 11, pp. 6797–6808, Nov. 2015.

[34] E. D. Azad, S. Gadoue, D. Atkinson, H. Slater, P. Barrass, and F. Blaabjerg, "Sensorless control of IM based on stator-voltage MRAS for limp-home EV applications," *IEEE Trans. Power Electron.*, vol. 33, no. 3, pp. 1911–1921, Mar. 2018.

[35] M. Korzonek, G. Tarchala, and T. O. Kowalska, "Simple stability enhancement method for stator current error-based MRAS-type speed estimator for induction motor drive," *IEEE Trans. Ind. Electron.*, vol. 67, no. 7, pp. 5854–5866, Jul. 2020.

[36] C. Du, Z. Yin, Y. Zhang, J. Liu, X. Sun, and Y. Zhong, "Research on active disturbance rejection control with parameter autotune mechanism for induction motors based on adaptive particle swarm optimization algorithm with dynamic inertia weight," *IEEE Trans. Power Electron.*, vol. 34, no. 3, pp. 2841–2855, Mar. 2019.

[37] S. M. Gadoue, D. Giaouris, and J. W. Finch, "MRAS sensorless vector control of an induction motor using new sliding-mode and fuzzy-logic adaptation mechanisms," *IEEE Trans. Energy Convers.*, vol. 25, no. 2, pp. 394–402, Jun. 2010.

[38] C. Y. Hung, P. Liu, and K. Y. Lian, "Fuzzy virtual reference model sensorless tracking control for linear induction motors," *IEEE Trans. Cybern.*, vol. 43, no. 3, pp. 970–981, Jun. 2013.

[39] H. Luo, Y. Lv, X. Deng, and H. Zhang, "Optimization of adaptation gains of full-order flux observer in sensorless induction motor drives using genetic algorithm," *Inf. Technol. J.*, vol. 8, no. 4, pp. 577–582, 2009.

[40] S. M. Gadoue, D. Giaouris, and J. W. Finch, "Sensorless control of induction motor drives at very low and zero speeds using neural network flux observers," *IEEE Trans. Ind. Electron.*, vol. 56, no. 8, pp. 3029–3039, Aug. 2009.

[41] B. Karanayil, M. F. Rahman, and C. Grantham, "Online stator and rotor resistance estimation scheme using artificial neural networks for vector controlled speed sensorless inductionmotor drive," *IEEE Trans. Ind. Electron.*, vol. 54, no. 1, pp. 167–176, Feb. 2007.

[42] J. Thomas and A. Hansson, "Speed tracking of a linear induction motor-enumerative nonlinear model predictive control," *IEEE Trans. Control Syst. Technol.*, vol. 21, no. 5, pp. 1956–1962, Sep. 2013.

[43] S. Golestan, J. M. Guerrero, and J. C. Vasquez, "Three-phase PLLs: A review of recent advances," *IEEE Trans. Power Electron.*, vol. 32, no. 3, pp. 1894–1907, Mar. 2017.

[44] S. Golestan, J. M. Guerrero, and J. C. Vasquez, "Single-phase PLLs: A review of recent advances," *IEEE Trans. Power Electron.*, vol. 32, no. 12, pp. 9013–9030, Dec. 2017.

[45] S. Golestan, M. Monfared, F. D. Freijedo, and J. M. Guerrero, "Advantages and challenges of a type-3 PLL," *IEEE Trans. Power Electron.*, vol. 28, no. 11, pp. 4985–4997, Nov. 2013.

[46] M. Preindl and E. Schaltz, "Sensorless model predictive direct current control using novel second-order PLL observer for PMSM drive systems," *IEEE Trans. Ind. Electron.*, vol. 58, no. 9, pp. 4087–4095, Sep. 2011.

[47] G. Wang, Z. Li, G. Zhang, Y. Yu, and D. Xu, "Quadrature PLL-based high-order sliding-mode observer for IPMSM sensorless control with online MTPA control strategy," *IEEE Trans. Energy Convers.*, vol. 28, no. 1, pp. 214–224, Mar. 2013.

[48] G. Wang, R. Yang, and D. Xu, "DSP-based control of sensorless IPMSM drives for wide-speed-range operation," *IEEE Trans. Ind. Electron.*, vol. 60, no. 2, pp. 720–727, Feb. 2013.

[49] G. Wang, T. Li, G. Zhang, X. Gui, and D. Xu, "Position estimation error reduction using recursive-least-square adaptive filter for model based sensorless interior permanent-magnet synchronous motor drives," *IEEE Trans. Ind. Electron.*, vol. 61, no. 9, pp. 5115–5125, Sep. 2014.

[50] G. Wang, H. Zhan, G. Zhang, X. Gui, and D. Xu, "Adaptive compensation method of position estimation harmonic error for EMF-based observer in sensorless IPMSM drives," *IEEE Trans. Power Electron.*, vol. 29, no. 6, pp. 3055–3064, Jun. 2014.

[51] G. Zhang, G. Wang, D. Xu, R. Ni, and C. Jia, "Multiple-AVF cross-feedback-network-based position error harmonic fluctuation elimination for sensorless IPMSM drives," *IEEE Trans. Ind. Electron.*, vol. 63, no. 2, pp. 821–831, Feb. 2016.

[52] G. Zhang, G. Wang, D. Xu, and N. Zhao, "ADALINE-network-based PLL for position sensorless interior permanent magnet synchronous motor drives," *IEEE Trans. Power Electron.*, vol. 31, no. 2, pp. 1450–1460, Feb. 2016.

[53] M. H. Bierhoff, "A general PLL-type algorithm for speed sensorless control of electrical drives," *IEEE Trans. Ind. Electron.*, vol. 64, no. 12, pp. 9253–9260, Apr. 2017.

[54] R. Antonello, L. Ortombina, F. Tinazzi, and M. Zigliotto, "Enhanced low-speed operations for sensorless anisotropic PM synchronous motor drives by a modified back-EMF observer," *IEEE Trans. Ind. Electron.*, vol. 65, no. 4, pp. 3069–3076, Apr. 2018.

[55] C. Gu, X. Wang, X. Shi, and Z. Deng, "A PLL-based novel commutation correction strategy for a high-speed brushless DC motor sensorless drive system," *IEEE Trans. Ind. Electron.*, vol. 65, no. 5, pp. 3752–3762, May 2018.

[56] M. W. K. Mbukani and N. Gule, "PLL-based sliding mode observer estimators for sensorless control of rotor-tied DFIG systems," *IEEE Trans. Ind. Appl.*, vol. 55, no. 6, pp. 5960–5970, Nov./Dec. 2019.

[57] Z. Xu, T. Zhang, Y. Bao, H. Zhang, and C. Gerada, "A nonlinear extended state observer for rotor position and speed estimation for sensorless IPMSM drives," *IEEE Trans. Power Electron.*, vol. 35, no. 1, pp. 733–743, Jan. 2020.

[58] Q. An, J. Zhang, Q. An, X. Liu, A. Shamekov, and K. Bi, "Frequency-adaptive complex-coefficient filter based enhanced sliding mode observer for sensorless control of permanent magnet synchronous motor drives," *IEEE Trans. Ind. Appl.*, vol. 56, no. 1, pp. 335–343, Jan./Feb. 2020.

[59] C. Lascu and G. D. Andreescu, "PLL position and speed observer with integrated current observer for sensorless PMSM drives," *IEEE Trans. Ind. Electron.*, vol. 67, no. 7, pp. 5990–5999, Jul. 2020.

[60] H. X. Nguyen, T. N. Tran, J. W. Park, N. V. P. Tran, and J. W. Jeon, "Improving the accuracy of battery-free multiturn absolute magnetic encoders by using a self-referencing lookup table algorithm," *IEEE Trans. Instrum. Meas.*, vol. 69, no. 8, pp. 5468–5477, Aug. 2020.

[61] F. Lei and M. H. White, "Reference injected phase-locked loops (PLL-RIs)," *IEEE Trans. Circuits Syst. I, Reg. Papers*, vol. 64, no. 7, pp. 1651–1660, Jul. 2017.

[62] P. Rodriguez, A. Luna, R. S. M. Aguilar, I. E. Otadui, R. Teodorescu, and F. Blaabjerg, "A stationary reference frame grid synchronization system for three-phase grid-connected power converters under adverse grid conditions," *IEEE Trans. Power Electron.*, vol. 27, no. 1, pp. 99–112, Jan. 2012.

[63] P. Rodriguez, A. Luna, I. Candela, R. Mujal, R. Teodorescu, and F. Blaabjerg, "Multiresonant frequency-locked loop for grid synchronization of power converters under distorted grid conditions," *IEEE Trans. Ind. Electron.*, vol. 58, no. 1, pp. 127–138, Jan. 2011.

[64] P. Rodriguez, A. Luna, M. Ciobotaru, R. Teodorescu, and F. Blaabjerg, "Advanced grid synchronization system for power converters under unbalanced and distorted operating conditions," in *Proc. IEEE 32nd Ind. Electron. Soc.*, 2006, pp. 5173–5178.

[65] Z. Xin, P. C. Loh, X. Wang, F. Blaabjerg, and Y. Tang, "Highly accurate derivatives for LCL-filtered grid converter with capacitor voltage active damping," *IEEE Trans. Power Electron.*, vol. 31, no. 5, pp. 3612–3625, May 2016.

[66] Z. Xin, R. Zhao, F. Blaabjerg, L. Zhang, and P. C. Loh, "An improved flux observer for field-oriented control of induction motors based on dual second-order generalized integrator frequency-locked loop," *IEEE J. Emerg. Sel. Top. Power Electron.*, vol. 5, no. 1, pp. 513–525, Mar. 2017.

[67] R. Zhao, Z. Xin, P. C. Loh, and F. Blaabjerg, "A novel flux estimator based on multiple second-order generalized integrators and frequency-locked loop for induction motor drives," *IEEE Trans. Power Electron.*, vol. 32, no. 8, pp. 6286–6296, Aug. 2017.

[68] S. Golestan, J. M. Guerrero, J. C. Vasquez, A. M. Abusorrah, and Y. A. Turki, "Modeling, tuning, and performance comparison of second-order-generalized-integrator-based FLLs," *IEEE Trans. Power Electron.*, vol. 33, no. 12, pp. 10229–10239, Dec. 2018.

[69] S. Golestan, J. M. Guerrero, J. C. Vasquez, A. M. Abusorrah, and Y. A. Turki, "A study on three-phase FLLs," *IEEE Trans. Power Electron.*, vol. 34, no. 1, pp. 213–224, Jan. 2019.

[70] S. Golestan, J. M. Guerrero, F. Musavi, and J. C. Vasquez, "Single-phase frequency-locked loops: A comprehensive review," *IEEE Trans. Power Electron.*, vol. 34, no. 12, pp. 11791–11812, Dec. 2019.

[71] S. Golestan, J. M. Guerrero, and J. C. Vasquez, "Is using a complex control gain in three-phase FLLs reasonable?," *IEEE Trans. Ind. Electron.*, vol. 67, no. 3, pp. 2480–2484, Mar. 2020.

[72] C. A. Busada, S. G. Jorge, A. E. Leon, and J. A. Solsona, "Current controller based on reduced order generalized integrators for distributed generation systems," *IEEE Trans. Ind. Electron.*, vol. 59, no. 7, pp. 2898–2909, Jul. 2012.

[73] P. Cheng and H. Nian, "Collaborative control of DFIG system during network unbalance using reduced-order generalized integrators," *IEEE Trans. Energy Convers.*, vol. 30, no. 2, pp. 453–464, Jun. 2015.

[74] S. Jiao, K. R. R. Potti, K. Rajashekara, and S. K. Pramanick, "A novel DROGI-based detection scheme for power quality improvement using four-leg converter under unbalanced loads," *IEEE Trans. Ind. Appl.*, vol. 56, no. 1, pp. 815–825, Jan./Feb. 2020.

[75] H. Wang and X. Ge, "Type-3 PLL based speed estimation scheme for sensorless linear induction motor drives," in *Proc. IEEE Conf. Power Electron.*, 2019, pp. 1303–1308.

[76] A. Bamigbade, V. Khadkikar, and M. A. Hosani, "A type-3 PLL for single-phase applications," in *Proc. Conf. IEEE IAS Annu. Meeting*, 2019, pp. 1–6.

[77] H. X. Nguyen, T. N. Tran, J. W. Park, and J. W. Jeon, "An adaptive linear-neuron-based third-order PLL to improve the accuracy of absolute magnetic encoders," *IEEE Trans. Ind. Electron.*, vol. 66, no. 6, pp. 4639–4649, Jun. 2019.

[78] M. K. Ghartemani, B. Ooi, and A. Bakhshai, "Application of enhanced phase-locked loop system to the computation of synchrophasors," *IEEE Trans. Power Del.*, vol. 26, no. 1, pp. 22–32, Jan. 2011.

[79] S. Bifaretti, P. Zanchetta, and E. Lavopa, "Comparison of two three-phase PLL systems for more electric aircraft converters," *IEEE Trans. Power Electron.*, vol. 29, no. 12, pp. 6810–6820, Dec. 2014.

[80] S. Golestan, J. M. Guerrero, and J. C. Vasquez, "Steady-state linear kalman filter-based PLLs for power applications: A second look," *IEEE Trans. Ind. Electron.*, vol. 65, no. 12, pp. 9795–9800, Dec. 2018.

[81] H. Wang, Y. Yang, X. Ge, S. Li, and Y. Zuo, "Speed-sensorless control of linear induction motor based on the SSLKF-PLL speed estimation scheme," *IEEE Trans. Ind. Appl.*, vol. 56, no. 5, pp. 4986–5002, Sep./Oct. 2020.

[82] H. Machida, M. Kambara, K. Tanaka, and F. Kobayashi, "A motor speed control system using a hybrid of dual-loop PLL and feed-forward," in *Proc. Int. Workshop Adv. Motion Control AMC*, 2010, pp. 185–190.

[83] H. Mchida, M. Kambara, K. Tanaka, and F. Kobayashi, "A motor speed control system using dual-loop PLL and speed feed-forward/back," in *Proc. Int. Conf. Mechatronics Autom.*, 2010, pp. 1512–1517.

[84] C. K. Aravind, B. I. Rani, C. Manickam, J. M. Guerrero, S. I. Ganesan, and C. Nagamani, "Performance evaluation of type-3 PLLs under wide variation in input voltage and frequency," *IEEE J. Emerg. Sel. Top. Power Electron.*, vol. 5, no. 3, pp. 971–981, Sep. 2017.

[85] H. Wang and X. Ge, "Multiple-complex-vector-filter-based phase-locked loop synchronization technique for seneorless linear induction motor drive system," in *Proc. IEEE Transport. Electrific. Conf. Expo*, 2019, pp. 1–6.

[86] B. I. Rani, C. K. Aravind, G. S. Ilango, and C. Nagamani, "A three phase PLL with a dynamic feed forward frequency estimator for synchronization of grid connected converters under wide frequency variations," *Int. J. Elect. Power Energy Syst.*, vol. 41, no. 1, pp. 63–70, Oct. 2012.

[87] G. Liu, H. Zhang, and X. Song, "Position estimation deviation suppression technology of PMSM combining phase self-compensation SMO and feed-forward PLL," *IEEE J. Emerg. Sel. Top. Power Electron.*, vol. 9, no. 1, pp. 335–344, Feb. 2021.

[88] F. Liccardo, P. Marino, and G. Raimondo, "Robust and fast three-phase PLL tracking system," *IEEE Trans. Ind. Electron.*, vol. 58, no. 1, pp. 221–231, Jan. 2011.

[89] S. Golestan, M. Ramezani, and J. M. Guerrero, "An analysis of the PLLs with secondary control path," *IEEE Trans. Ind. Electron.*, vol. 61, no. 9, pp. 4824–4828, Sep. 2014.

[90] T. N. Tran, H. X. Nguyen, J. W. Park, and J. W. Jeon, "Improving the accuracy of an absolute magnetic encoder by using harmonic rejection and a dual phase-locked loop," *IEEE Trans. Ind. Electron.*, vol. 66, no. 7, pp. 5476–5486, Jul. 2019.

[91] H. Wang, X. Ge, Y. Yue, and Y. Liu, "Dual phase-locked loop based speed estimation scheme for sensorless vector control of linear induction motor drives," *IEEE Trans. Ind. Electron.*, vol. 67, no. 7, pp. 5900–5912, Jul. 2020.

[92] E. Robles, S. Ceballos, J. Pou, J. Martin, J. Zaragoza, and P. Ibanez, "Variable-frequency grid sequence detector based on a quasi-ideal low pass filter stage and a phase-locked loop," *IEEE Trans. Power Electron.*, vol. 25, no. 10, pp. 2552–2563, Oct. 2010.

[93] F. G. Espin, E. Figueres, and G. Garcera, "An adaptive synchronous-reference-frame phase-locked loop for power quality improvement in a polluted utility grid," *IEEE Trans. Ind. Electron.*, vol. 59, no. 6, pp. 2718–2731, Jun. 2012.

[94] F. A. S. Neves, H. Souza, M. Cavalcanti, F. Bradaschia, and E. Bueno, "Digital filters for fast harmonic sequence components separation of unbalanced and distorted three-phase signals," *IEEE Trans. Ind. Electron.*, vol. 59, no. 10, pp. 3847–3859, Oct. 2012.

[95] A. F. Zobaa and S. H. E. A. Aleem, "A new approach for harmonic distortion minimization in power systems supplying nonlinear loads," *IEEE Trans. Ind. Informat.*, vol. 10, no. 2, pp. 1401–1412, May 2014.

[96] S. Golestan, J. M. Guerrero, and G. Gharehpetian, "Five approaches to deal with problem of DC offset in phase-locked loop algorithms: Design considerations and performance evaluations," *IEEE Trans. Power Electron.*, vol. 31, no. 1, pp. 648–660, Jan. 2016.

[97] S. Golestan, J. M. Guerrero, and J. C. Vasquez, "DC-offset rejection in phase-locked loops: A novel approach," *IEEE Trans. Ind. Electron.*, vol. 63, no. 8, pp. 4942–4946, Aug. 2016.

[98] P. Kanjiya, V. Khadkikar, and M. S. E. Moursi, "Adaptive low-pass filter based DC offset removal technique for three-phase PLLs," *IEEE Trans. Ind. Electron.*, vol. 65, no. 11, pp. 9025–9029, Nov. 2018.

[99] S. Gude and C. Chu, "Dynamic performance enhancement of single-phase and two-phase enhanced phase-locked loops by using in-loop multiple delayed signal cancellation filters," *IEEE Trans. Ind. Appl.*, vol. 56, no. 1, pp. 740–751, Jan./Feb. 2020.

[100] S. Golestan, "Modeling, analyzing, and designing advanced synchronization techniques for power converters," Ph.D. dissertation, Dept. Energy Technol.,Aalborg Univ., Aalborg, Denmark, 2018.

[101] C. Lascu, I. Boldea, and F. Blaabjerg, "A modified direct torque control for induction motor sensorless drive," *IEEE Trans. Ind. Appl.*, vol. 36, no. 1, pp. 122–130, Jan./Feb. 2000.

[102] H. Wang, Y. Yang, D. Chen, X. Ge, S. Li, and Y. Zuo, "Speed-sensorless control of induction motors with an open-loop synchronization method," *IEEE J. Emerg. Sel. Topics Power Electron.*, to be published, doi: 10.1109/JESTPE.2021.3050805.

[103] C. Lascu, I. Boldea, and F. Blaabjerg, "Direct torque control of sensorless induction motor drives: A sliding-mode approach," *IEEE Trans. Ind. Appl.*, vol. 40, no. 2, pp. 582–590, Mar./Apr. 2004.

[104] C. Lascu and G. D. Andreescu, "Sliding-mode observer and improved integrator with DC-offset compensation for flux estimation in sensorless-controlled induction motors," *IEEE Trans. Ind. Electron.*, vol. 53, no. 3, pp. 785–794, Jun. 2006.

[105] C. Lascu, I. Boldea, and F. Blaabjerg, "A class of speed-sensorless sliding-mode observers for high-performance induction motor drives," *IEEE Trans. Ind. Electron.*, vol. 56, no. 9, pp. 3394–3403, Sep. 2009.

[106] Z. Xin, X. Wang, Z. Qin, M. Lu, P. C. Loh, and F. Blaabjerg, "An improved second-order generalized integrator based quadrature signal generator," *IEEE Trans. Power Electron.*, vol. 31, no. 12, pp. 8068–8073, Dec. 2016.

[107] H. Wang, Y. Yang, Y. Zuo, S. Li, X. Hu, and X. Ge, "A speed estimation scheme based on an improved SOGI-FLL for speed-sensorless control of induction motor drives," in *Proc. 46th Annu. Conf. IEEE Ind. Electron. Soc.*, 2020, pp. 852–857.

[108] M. K. Ghartemani, S. A. Khajehoddin, P. K. Jain, A. Bakhshai, and M. Mojiri, "Addressing DC component in PLL and notch filter algorithms," *IEEE Trans. Power Electron.*, vol. 27, no. 1, pp. 78–86, Jan. 2012.

[109] C. Zhang, X. Zhao, X. Wang, X. Chai, Z. Zhang, and X. Guo, "A grid synchronization PLL method based on mixed second- and third-order generalized integrator for DC offset elimination and frequency adaptability," *IEEE J. Emerg. Sel. Topics Power Electron.*, vol. 6, no. 3, pp. 1517–1526, Sep. 2018.

[110] S. Golestan, E. Ebrahimzadeh, J. M. Guerrero, and J. C. Vasquez, "An adaptive resonant regulator for single-phase grid-tied VSCs," *IEEE Trans. Power Electron.*, vol. 33, no. 2, pp. 1867–1873, Mar. 2018.

[111] S. Vazquez, J. A. Sanchez, M. R. Reyes, J. I. Leon, and J. M. Carrasco, "Adaptive vectorial filter for grid synchronization of power converters under unbalanced and/or distorted grid conditions," *IEEE Trans. Ind. Electron.*, vol. 61, no. 3, pp. 1355–1367, Mar. 2014.

[112] X. Guo, W. Wu, and Z. Chen, "Multiple-complex coefficient-filter-based phase-locked loop and synchronization technique for three-phase grid interfaced converters in distributed utility networks," *IEEE Trans. Ind. Electron.*, vol. 58, no. 4, pp. 1194–1204, Apr. 2011.

[113] W. Li, X. Ruan, C. Bao, D. Pan, and X. Wang, "Grid synchronization systems of three-phase grid-connected power converters: A complex-vector-filter perspective," *IEEE Trans. Ind. Electron.*, vol. 61, no. 4, pp. 1855–1870, Apr. 2014.

[114] G. Wang *et al.*, "Enhanced position observer using second-order generalized integrator for sensorless interior permanent magnet synchronous motor drives," *IEEE Trans. Energy Convers.*, vol. 29, no. 2, pp. 486–495, Jun. 2014.

[115] J. Matas, M. Castilla, J. Miret, L. G. Vicua, and R. Guzman, "An adaptive pre-filtering method to improve the speed/accuracy trade-off of voltage sequence detection methods under adverse grid conditions," *IEEE Trans. Ind. Electron.*, vol. 61, no. 5, pp. 2139–2151, May 2014.

[116] H. Liu, Y. Xing, and H. Hu, "Enhanced frequency-locked loop with a comb filter under adverse grid conditions," *IEEE Trans. Power Electron.*, vol. 31, no. 12, pp. 8046–8051, Dec. 2016.
[117] N. Kumar, I. Hussain, B. Singh, and B. K. Panigrahi, "Implementation of multilayer fifth-order generalized integrator-based adaptive control for grid-tied solar PV energy conversion system," *IEEE Trans. Ind. Informat.*, vol. 14, no. 7, pp. 2857–2868, Jul. 2018.
[118] G. Zhang, X. Yang, G. Wang, and D. Xu, "Position error fluctuation elimination for model-based self-sensing IPMSM drives incorporating ROGI decoupling network," in *Proc. Conf. Electric. Mach. Syst.*, 2019, pp. 1–6.

Huimin Wang (Student Member, IEEE) received the B.Eng. and Ph.D. degrees in electrical engineering from Southwest Jiaotong University, Chengdu, China, in 2016 and 2021, respectively.

From 2019 to 2020, he has been a Visiting Ph.D. student with the Department of Energy Technology, Aalborg University, Aalborg, Denmark. His research interests include motor drive system and its speed-sensorless control and synchronization techniques in grid-connected system.

Dr. Wang was a recipient of the Best Paper Award of IEEE Transportation Electrification Conference and EXPO Asia-Pacific in 2019.

Yongheng Yang (Senior Member, IEEE) received the B.Eng. degree in electrical engineering and automation from Northwestern Polytechnical University, Xi'an, China, in 2009, and the Ph.D. degree in energy technology (power electronics and drives) from Aalborg University, Aalborg, Denmark, in 2014.

From September 2009 to August 2011, he took part in the Postgraduate Training Program with Southeast University, China. In 2013, he spent three months as a Visiting Scholar with Texas A&M University, USA. Since 2014, he has been with the Department of Energy Technology, Aalborg University, where he became a tenured Associate Professor in 2018. In January 2021, he joined Zhejiang University, China, where he is currently a ZJU100 Professor with the Institute of Power Electronics, College of Electrical Engineering. His current research interests include the grid–integration of photovoltaic systems and control of power converters, in particular, the mechanism and control of grid-forming power converters and systems.

Dr. Yang was the Chair of the IEEE Denmark Section (2019–2020). He is an Associate Editor for several IEEE Transactions/Journals. He is a Deputy Editor for the *IET Renewable Power Generation for Solar Photovoltaic Systems*. He was the recipient of the 2018 IET Renewable Power Generation Premium Award and was an Outstanding Reviewer for the IEEE TRANSACTIONS ON POWER ELECTRONICS in 2018. He was a recipient of the 2021 Richard M. Bass Outstanding Young Power Electronics Engineer Award from the IEEE Power Electronics Society (PELS) and two IEEE Best Paper Awards. He is currently the Secretary of the IEEE PELS Technical Committee on Sustainable Energy Systems.

Xinglai Ge (Member, IEEE) received the B.S., M.S., and Ph.D. degrees in electrical engineering from Southwest Jiaotong University, Chengdu, China, in 2001, 2004, and 2010, respectively.

From 2013 to 2014, he was a Visiting Scholar with the School of Electrical and Computer Engineering, Georgia Institute of Technology, Atlanta, GA, USA. He is currently a Full Professor with the School of Electrical Engineering, Southwest Jiaotong University, and the Vice Director of Department of Power Electronics and Power Drive. He is the author and co-author of more than 60 technical papers. His research interests include stability analysis and control of electrical traction system, fault diagnosis and reliability evaluation of traction converter, and motor drive system.

Yun Zuo (Student Member, IEEE) received the B. Eng. degree in electrical engineering and automation from Dalian Jiaotong University, Dalian, China, in 2019. He is currently working toward the Ph.D. degree in electrical engineering with Southwest Jiaotong University, Chengdu, China.

His research interests include motor drives and its speed-sensorless control.

Yan Yue received the B.Eng. degree in electrical engineering and automation from Dalian Jiaotong University, Dalian, China, in 2016, and the M.Eng. degree in electrical engineering from Southwest Jiaotong University, Chengdu, China, in 2019.

He is currently working as an Engineer with China Railway Eryuan Engineering Group Company Ltd, Chengdu. His research interests include permanent magnet synchronous motor drives and traction grid modeling.

Songtao Li received the B.Eng. degree from the Lanzhou University of Technology, Lanzhou, China, in 2018, and the M.Eng. degree from Southwest Jiaotong University, Chengdu, China, in 2021, both in electrical engineering.

He is currently an Engineer with Xi'an Huawei Digital Power Technologies Company LTD, Xi'an, China. His current research interests include permanent magnet synchronous motor drives and automotive powertrains.